

# A relativistic model of b-EMRI systems and their gravitational radiation

Yucheng Yin,<sup>1,2</sup> Josh Mathews,<sup>3</sup> Alvin J. K. Chua,<sup>3,4</sup> and Xian Chen<sup>1,2,\*</sup>

<sup>1</sup>*Department of Astronomy, School of Physics, Peking University, 100871 Beijing, China*  
<sup>2</sup>*Kavli Institute for Astronomy and Astrophysics at Peking University, 100871 Beijing, China*

<sup>3</sup>*Department of Physics, National University of Singapore, Singapore 117551*

<sup>4</sup>*Department of Mathematics, National University of Singapore, Singapore 119076*

(Dated: October 15, 2024)

A binary extreme-mass-ratio inspiral (b-EMRI) is a hierarchical triple system consisting of a stellar-mass binary black hole (BBH) orbiting a central Kerr supermassive black hole (SMBH). Although predicted by several astrophysical models, b-EMRIs pose a challenge in waveform modeling due to their complex three-body dynamics and strong relativistic effects. Here we take advantage of the hierarchical nature of b-EMRI systems to transform the internal motion of the small binary into global trajectories around the SMBH. This allows us to use black hole perturbation theory to calculate both the low-frequency gravitational waveform due to its EMRI nature and the high-frequency waveform generated by the inner motion of the BBH. When the inner binary’s separation vanishes, our calculation recovers the standard relativistic adiabatic EMRI waveform. Furthermore, by including the high-frequency perturbation, we find a correction to the waveform as large as the adiabatic order when the frequency matches the quasinormal modes (QNMs) of the SMBH, therefore supporting an earlier proof-of-concept study claiming that the small BBH can resonantly excite the QNMs of the SMBH. More importantly, we find that b-EMRIs can evolve faster than regular EMRIs due to this resonant dissipation through the high-frequency modes. These characteristics distinguish b-EMRI waveform templates from regular EMRI templates for future space-based gravitational-wave detectors.

## I. INTRODUCTION

Extreme-mass-ratio inspirals (EMRIs) are an important target for future milli-Hertz gravitational-wave (GW) detectors, such as the Laser Interferometer Space Antenna (LISA) [1, 2], or China’s Taiji [3] and Tian-Qin [4, 5] projects. An EMRI normally consists of a stellar-mass black hole (BH) or neutron star (the ‘secondary’) and a SMBH (the ‘primary’). The mass ratio  $\epsilon$  of the two bodies falls in a typical range between  $10^{-6}$  and  $10^{-3}$ . By studying the GWs radiated during the last  $\mathcal{O}(1/\epsilon)$  orbits before plunge [6], we can measure the spin and mass of the central SMBH, and test the Kerr metric with unprecedented precision [7–11]. There has been significant efforts in developing both approximate and fully relativistic EMRI waveform models over the years, e.g. [12–23], including many works on the finite size effects of the compact secondary body [24–38]. Recent astrophysical models predict that the small body in an EMRI, in fact, could be a stellar-mass BBH. Such a BBH could be either captured by the SMBH during a close tidal interaction [39, 40], or delivered to the vicinity of the SMBH by an accretion disk if the SMBH happens to be inside an active galactic nucleus (AGN) [41–44]. In such a triple system, the BBH is often referred to as the “inner binary” (IB), and the binary formed by the IB and the SMBH is called the “outer binary” (OB). Since the small BH binary is now spiraling into the SMBH, the whole system is now known as the “binary EMRI” (or

b-EMRI for short [40, 45]).

While solid observational evidence for b-EMRIs is currently lacking, it has been suggested that the event GW190521, discovered in the third observing run of the Laser Interferometer GW Observatory (LIGO) and the Virgo detectors [46, 47], could have derived from a BBH merger in vicinity of a SMBH. In particular, this event involves one of the most massive BBHs ever detected, whose final mass is approximately  $150M_{\odot}$ , far greater than the typical mass of the BHs found in Galactic X-ray binaries [48, 49]. The high mass could be explained by a redshift of the GW signal if the merger happened very close to a SMBH [50]. Moreover, a potentially associated AGN flare is reported by the Zwicky Transient Facility [51] and further analysis of the flare [52] suggests that GW190521 could come from the accretion disk of that AGN.

The possibility of forming b-EMRIs in astrophysical environments has inspired many studies on the waveform of such a special GW source. The methods adopted by these earlier studies can be broadly divided into two categories. The first approach starts from the waveform of an isolated stellar-mass BBH and adds to it relativistic effects to account for the existence of a nearby SMBH [53]. Previously considered effects include Doppler and gravitational redshifts [54–58], aberration due to the fast motion of the BBH [59, 60], and gravitational lensing of the GW signal by the SMBH either in the geometric optics limit [61] or the wave optics one [62]. An important ingredient that is missing by these works is the gravitational radiation of the OB, i.e., the EMRI signal.

The second approach starts with a standard EMRI and replaces the stellar-mass secondary with a BBH. The original idea is to model the small binary as two

---

\* Corresponding author.  
xian.chen@pku.edu.cn

point particles orbiting each other with a centre-of-mass that is in turn orbiting the SMBH. The waveform is then computed using the Teukolsky formalism [63, 64]. More recently, Ref. [65] took a slightly different approach, viewing the BBH in a b-EMRI as a mass distribution with spin and other finite size effects and assessed the distinguishability of b-EMRI waveforms from standard EMRI systems. This perspective leverages the Mathisson-Papapetrou-Dixon-Harte formalism [66–71], already used extensively to describe finite size effects of the secondary in EMRI models. If we were to ‘skeletonize’ the extended stress-energy distribution of two orbiting point particles about a reference worldline via a multipole expansion, then it becomes more apparent how the approach relates to the MPD-Harte formalism. Further extension of this method is used to study “dirty EMRIs” [72]. Additionally, some efforts have been made to modify the “numerical kludge” (NK) waveform templates to mimic the GW signals of b-EMRIs [73].

Two problems remain unsolved in the modeling of b-EMRI waveforms. First, Ref. [63, 64, 73] treat the trajectories of the small BHs as an algebraic addition of the inner and outer orbits. Although intuitive, this addition is invalid for motions in the relativistic regime. Both special relativistic effects, such as the high velocity of the IB, and general relativistic effects, like the curvature of spacetime, can cause the circular inner orbit observed from the centre-of-mass (CM) of the IB to appear distorted when viewed from infinity. A rigorous coordinate transformation to account for the above relativistic effects is needed.

The second problem is partially realized in Ref. [63] — that the inner motion of the small BHs could cause a perturbation which has almost the same frequency as one of the quasi-normal modes (QNMs) of the SMBH [74]. In this case, the IB can resonantly excite the SMBH as predicted by BH perturbation theory [63], but the effect requires precise treatment of the perturbing IB. For example, in Ref. [65], the resonant excitation of the QNMs was not observed as the high-frequency modes of the perturber were neglected. In that work, the IB is closer to merger, corresponding to higher values of the inner frequency that may have been too high to excite the QNMs. That study would need to be extended to larger separations of the IB to discern QNM excitation.

Recent dynamics models for b-EMRIs have made significant progress in describing the evolution of the IB and OB simultaneously [75–78]. The key idea is to solve the evolution in a frame in which the CM of the IB is in free fall. In this free-fall frame (FFF), by the equivalence principle, the evolution of the BBH is dominated by its self-gravity. For our purposes, a coordinate transformation from the FFF to the Boyer-Lindquist (BL) coordinates [79–81], in principle, should provide us with the trajectories of the two small BHs around the SMBH. We can isolate the high-frequency components of the trajectories due to the inner motion of the IB and evaluate their excitation of the QNMs. We use this scheme to

produce a relativistic b-EMRI waveform model.

Typical EMRI models employ a multi-scale (or two-timescale) expansion [6, 82, 83]. Within the multi-scale framework, the resulting waveforms are labelled by the accuracy of the waveform phase. This follows from the foundational scaling argument in Ref. [6], that showed that the average waveform phase has the asymptotic small mass-ratio expansion

$$\phi = \epsilon^{-1}\phi^{(0)} + \epsilon^0\phi^{(1)} + \mathcal{O}(\epsilon). \quad (1)$$

The first term is labelled as ‘adiabatic order’ (OPA) and the subsequent subleading terms are ‘ $n^{\text{th}}$  post-adiabatic order’ (nPA). For simplicity, we neglect discussion of orbital resonances which include phase terms scaling with  $\epsilon^{-1/2}, \epsilon^{1/2}$  etc. For EMRI parameter estimation, it is anticipated that 1PA accurate models should be sufficient [2, 83]. In the model in this work, the b-EMRI parameters formally distinguish the waveform from a regular EMRI in a phase term that scales as  $(d/M)^2\epsilon^{-1}$ , where  $d$  is the diameter of the IB’s orbit. The stability of the b-EMRI implies that  $(d/M)^2 \approx \epsilon$ , meaning that the distinguishing phase term effectively scales equivalently to a 1PA phase correction. However, we find that resonances between the IB’s orbital frequency and the SMBH’s QNMs can cause the b-EMRI phase correction to grow as large as a significant fraction of  $\phi^{(0)}$ .

This paper is organized as follows. In Sec. II we derive the trajectories of the small black holes using a series of coordinate transformations, starting from the FFF to the Local Inertia Frame (LIF) and finally to BL coordinates. We use these trajectories to expand the Teukolsky source term into a series expansion in the diameter of the IB. In addition, we present the schemes used to compute the waveform snapshots and adiabatic waveforms. In Sec. III, we describe the steps we take to compute the numerical waveform. In Sec. IV, we show the results from our model, including the fluxes, evolution of the OB, waveforms, and the properties of the QNMs in b-EMRI systems. In Sec. V, we compare our results with those presented in Ref. [63, 65, 73]. We also explore the parameter space to find stable b-EMRI systems and examine the validity of our model. Finally, in Sec. VI we summarize our main findings and outline potential directions for future studies. Throughout this paper, we set  $G = c = 1$ .

## II. THEORY

### A. Definition of model parameters

Fig. 1 shows the physical picture of a b-EMRI system. The central SMBH is a Kerr black hole with a mass of  $M \sim 10^5 - 10^8 M_\odot$  and a spin parameter of  $a$ . We denote  $p$  as the semi-latus rectum of the OB, which is equivalent to the radius of the OB if the orbit is circular. As for the IB, we denote the masses of the two stellar-mass BHs as

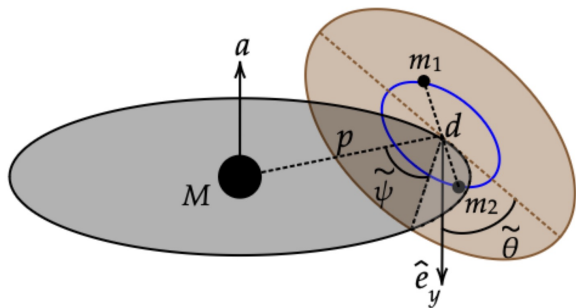


FIG. 1: A b-EMRI system and its parameters.

$M$	mass of SMBH $\sim 10^5 - 10^8 M_\odot$
$a$	spin of SMBH fixed at $0.9M$
$\epsilon$	mass ratio $\sim 10^{-6} - 10^{-3}$
$p$	outer radius scaled by $M$
$d$	diameter of IB scaled by $\mu = M\epsilon$
$\tilde{\psi}$	precession angle ranging from 0 to $2\pi$
$\tilde{\theta}$	inclination angle ranging from $-\pi/2$ to $\pi/2$

TABLE I: Key parameters of b-EMRI in this paper.

$m_1$  and  $m_2$ . We use  $\mu$  to represent the total mass of the IB so that  $\mu \equiv m_1 + m_2 = M\epsilon$ , and  $m$  is reserved to denote a multipole number, which is an integer. We assume  $m_1 = m_2$  and a circular orbit for the IB for simplicity and denote its diameter as  $d$ .

In the following, we will assume a Newtonian orbit for the inner orbital motion of the two stellar BHs, which requires that  $d$  is relatively large compared to  $\mu$  (e.g.,  $d > 1000\mu$ ). Other constraints on  $d$ ,  $\epsilon$ , and  $p$  will be discussed in detail in Sec. VB. There are two Euler angles determining the orientation of the IB and we will see how they function in Eq. (7), where  $\tilde{\psi}$  is the initial precession angle, which introduces a phase term in the waveform, and  $\tilde{\theta}$  is the inclination angle between the inner orbital plane and the outer one. We will see that  $\tilde{\theta}$  is relatively more important than  $\tilde{\psi}$  in affecting the b-EMRI waveform. In total there are seven parameters in our b-EMRI model. They are listed in Table I.

## B. Orbital motion of the outer binary

In this study we assume that the orbit of the OB follows a circular-equatorial orbit in Kerr spacetime, the metric of which is

$$ds^2 = - \left(1 - \frac{2Mr}{\Sigma}\right) dt^2 - \frac{4Mar \sin^2 \theta}{\Sigma} dt d\varphi + \frac{\Sigma}{\Delta} dr^2 + \Sigma d\theta^2 + \sin^2 \theta \left( r^2 + a^2 + \frac{2Ma^2 r \sin^2 \theta}{\Sigma} \right) d\varphi^2, \quad (2)$$

where  $\Delta = r^2 - 2Mr + a^2$  and  $\Sigma = 1/(\rho\bar{\rho})$  with  $\rho = (r - ia \cos \theta)^{-1}$ . Here overbar denotes complex conjugate. The complete form of the Kerr geodesics can be

found in Ref. [84–86], but here we focus on the circular-equatorial case, where the Carter constant  $\mathcal{Q}$  is set to zero. We express the geodesic equations in terms of the four-velocity  $u^x = dx/d\tau$  ( $x = t, r, \theta, \varphi$ ) as follows

$$u^t = \frac{\mathcal{E}}{p^2} \left[ \frac{(p^2 + a^2)^2}{\Delta} - a^2 \right] + \frac{a\mathcal{L}_z}{p^2} \left( 1 - \frac{p^2 + a^2}{\Delta} \right), \quad (3a)$$

$$u^r = 0 \quad (\text{with } r = p), \quad (3b)$$

$$u^\theta = 0 \quad (\text{with } \theta = \pi/2), \quad (3c)$$

$$u^\varphi = \frac{\mathcal{L}_z}{p^2} + \frac{a\mathcal{E}}{p^2} \left( \frac{p^2 + a^2}{\Delta} - 1 \right) - \frac{a^2 \mathcal{L}_z}{p^2 \Delta}, \quad (3d)$$

where  $\mathcal{E}$  and  $\mathcal{L}_z$  are dimensionless energy and angular momentum of the OB.

In the circular-equatorial case, the quantities  $\mathcal{E}$  and  $\mathcal{L}_z$  can be written as

$$\mathcal{E} \equiv \frac{E}{\mu} = \frac{p^{3/2} - 2Mp^{1/2} \pm aM^{1/2}}{p^{3/4} (p^{3/2} - 3Mp^{1/2} \pm 2aM^{1/2})^{1/2}}, \quad (4a)$$

$$\mathcal{L}_z \equiv \frac{L_z}{\mu} = \frac{\pm M^{1/2} (p^2 \mp 2aM^{1/2} p^{1/2} + a^2)}{p^{3/4} (p^{3/2} - 3Mp^{1/2} \pm 2aM^{1/2})^{1/2}}, \quad (4b)$$

where the upper signs correspond to a prograde outer orbit and lower signs to a retrograde one. Throughout the paper, we assume the IB orbit is prograde. These expressions can be derived from the radial component of the Kerr geodesic equations [84]

$$\Sigma^2 \left( \frac{dr}{d\tau} \right)^2 = [\mathcal{E}(p^2 + a^2) - a\mathcal{L}_z]^2 - \Delta [p^2 + (\mathcal{L}_z - a\mathcal{E})^2] \equiv R, \quad (5)$$

where we have assumed  $\mathcal{Q} = 0$ . By setting  $R = 0$  and  $R' \equiv \partial_p R = 0$  for a circular-equatorial orbit, we obtain Eq. (4).

## C. Coordinate transformation for the inner orbit

The relative motion of the two stellar-mass BHs can be solved most easily in a frame in which the binaries centre of mass is freely falling in the curved spacetime around the BBH (the aforementioned FFF). In this frame, the spacetime is sufficiently flat due to Einstein's Equivalence Principle, and hence the two BH follows a near-Keplerian orbit. Together with the previous assumption of a circular IB, we can calculate the inner orbital frequency as  $\omega_{IB} = \sqrt{\mu/d^3}$  and write the coordinates of the two BHs in their orbital plane as

$$\tilde{x} = \frac{1}{2} d \cos(\omega_{IB} \tau), \quad (6a)$$

$$\tilde{y} = 0, \quad (6b)$$

$$\tilde{z} = \frac{1}{2} d \sin(\omega_{IB} \tau), \quad (6c)$$

where  $\tau$  is the proper time of the FFF, and we have assumed equal mass for the inner binary so that the radius of the circular motion is  $d/2$ . Furthermore, to account for an arbitrary orientation of the IB, we use

$$\begin{bmatrix} x \\ y \\ z \end{bmatrix} = \begin{bmatrix} \cos \tilde{\psi} & 0 & -\sin \tilde{\psi} \\ 0 & 1 & 0 \\ \sin \tilde{\psi} & 0 & \cos \tilde{\psi} \end{bmatrix} \begin{bmatrix} 1 & 0 & 0 \\ 0 & \cos \tilde{\theta} & -\sin \tilde{\theta} \\ 0 & \sin \tilde{\theta} & \cos \tilde{\theta} \end{bmatrix} \begin{bmatrix} \tilde{x} \\ \tilde{y} \\ \tilde{z} \end{bmatrix}, \quad (7)$$

to rotate the orbital plane of the IB and get the coordinates in the FFF.

Since the Teukolsky formalism is derived in BL coordinates, we need to transform the motion of the small BHs from the FFF to BL coordinates. This transformation is done in two steps [80, 87]. The relationship between different coordinates are illustrated in Fig. 2.

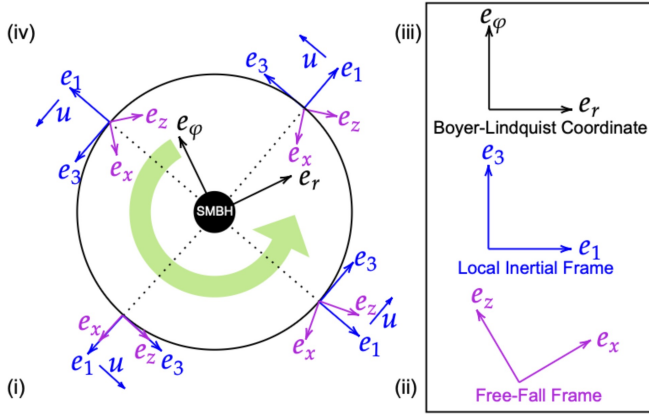


FIG. 2: Different reference frames used in this paper and their relative orientation as they rotate around the SMBH. It is a top view of Fig. 1 where  $e_1, e_2, e_3$  are unit bases with direction aligned with  $e_{X^1}, e_{X^2}, e_{X^3}$ .

First, we transform the inner motion into the LIF. This frame is moving at the same velocity as the FFF but its three spatial axes are aligned, respectively, with the  $\hat{e}_r, \hat{e}_\theta,$  and  $\hat{e}_\varphi$  axes of the BL coordinates. It has been shown that the spatial axes of the FFF and LIF differ by a precession, with an angular frequency of  $\Omega = -\sqrt{M/p^3}$  [87]. It happens to be the Keplerian orbital frequency in our circular-equatorial case. Consequently, coordinates in these two frames also differ by a rotation

$$T = \tau, \quad (8a)$$

$$X^1 = x \cos(\Omega\tau) - z \sin(\Omega\tau), \quad (8b)$$

$$X^2 = y, \quad (8c)$$

$$X^3 = x \sin(\Omega\tau) + z \cos(\Omega\tau). \quad (8d)$$

Second, we transform the coordinates in the LIF into the BL coordinates. Although the distance between each stellar-mass BH and the CM of the IB is fixed in the LIF (due to our assumption of circular inner orbit), in the BL coordinates the distance varies with time because of two reasons. (i) The coordinates in the LIF are measured by

an observer at the CM of the IB, while the BL coordinates are measured by an observer at infinity. There is a coordinate transformation between the two. (ii) Since the CM is moving, the coordinate transformation also varies with time. It is important to mention that such a variation of the distance from the CM has not been accounted for in the previous studies. This varying distance can be generally expanded into an infinite series of terms [81], and for our purposes it is sufficient to truncate the terms at the second order in  $X^{1,2,3}$ . The resulting trajectory of one small BH has been derived in Ref. [80] and can be written as

$$t = t_0 + \frac{(\mathcal{M}\mathcal{M}_\varphi + \gamma_{\varphi\varphi}^{1/2}\nu)X^3(\kappa_\varphi X^1 + 1)}{\gamma_{\varphi\varphi}^{1/2}\mathcal{M}/\gamma} + \frac{(\gamma_{\varphi\varphi}^{1/2} + \mathcal{M}\mathcal{M}_\varphi\nu)(T - \Omega X^1 X^3)}{\gamma_{\varphi\varphi}^{1/2}\mathcal{M}/\gamma}, \quad (9a)$$

$$r = r_0 + \frac{2X^1 + \kappa_r(X^1)^2 - \kappa_\theta(X^2)^2 - \kappa_\varphi(X^3)^2}{2\gamma_{rr}^{1/2}}, \quad (9b)$$

$$\theta = \theta_0 + \frac{\kappa_\theta X^1 X^2 + X^2}{\gamma_{\theta\theta}^{1/2}}, \quad (9c)$$

$$\varphi = \varphi_0 + \frac{X^3(\kappa_\varphi X^1 + 1) + \nu(T - \Omega X^1 X^3)}{\gamma_{\varphi\varphi}^{1/2}/\gamma}, \quad (9d)$$

where  $\mathcal{M}, \mathcal{M}_\varphi, \gamma_{rr}^{1/2}, \gamma_{\theta\theta}^{1/2}, \gamma_{\varphi\varphi}^{1/2}, \kappa_r, \kappa_\theta, \kappa_\varphi, \nu, \gamma$  are all functions of  $M, a, p$ . Detailed expressions for these functions are provided in Appendix A.

From Eqs. (7)-(9), the BL coordinate  $t, r, \theta, \varphi$  of each small BH can be expressed as a series expansion of  $d$ , which must be small to ensure the stability of the IB which we discuss in Sec. VB. The trajectory then takes the form of

$$t = c_{00} + c_{01}d + c_{02}d^2 + \mathcal{O}(d^3), \quad (10a)$$

$$r = c_{10} + c_{11}d + c_{12}d^2 + \mathcal{O}(d^3), \quad (10b)$$

$$\theta = c_{20} + c_{21}d + c_{22}d^2 + \mathcal{O}(d^3), \quad (10c)$$

$$\varphi = c_{30} + c_{31}d + c_{32}d^2 + \mathcal{O}(d^3), \quad (10d)$$

where the zeroth order terms  $c_{00}, c_{10}, c_{20},$  and  $c_{30}$  correspond to the outer motion with the geodetic relations:

$$c_{00} = u^t \tau, \quad (11a)$$

$$c_{10} = p, \quad (11b)$$

$$c_{20} = \pi/2, \quad (11c)$$

$$c_{30} = u^\varphi \tau. \quad (11d)$$

The first and second order coefficients  $c_{01}, c_{02}, c_{11}, c_{12}, c_{21}, c_{22}, c_{31}, c_{32}$  are derived in Appendix A. We note that  $c_{01}, c_{02}, c_{11}, c_{12}, c_{21}, c_{22}, c_{31}, c_{32}$  contain  $\omega_{IB} = \sqrt{\mu/d^3}$ , which is a function of  $d$ . However, we precalculate  $\omega_{IB}$  here and treat it as another independent parameter.

The expansion shown above reveals a much richer structure in the trajectory of each small BH than a simple addition of the inner and outer motion as assumed



previously in Ref. [63, 64, 73]. It allows us to more accurately account for the deviation of each small BH from geodesic motion and, in turn, compute the waveform resulting from the perturbed Kerr spacetime.

#### D. Teukolsky formalism

In this subsection, we review the Teukolsky-based Green function method for computing gravitational radiation within the framework of black hole perturbation theory. We refer our readers to Ref. [88] for an overview of the Teukolsky formalism. In addition, an analytical scheme of calculating the generic time-like Kerr geodesics can be found presented in Ref. [89], and the method of generating waveform snapshots for EMRIs on generic orbits is discussed in Ref. [90, 91].

The Teukolsky master equation provides a comprehensive framework for describing perturbations to Kerr spacetime [92, 93]. It is expressed as follows:

$$\begin{aligned} \mathcal{D}_s^2 \psi \equiv & \left[ \frac{(r^2 + a^2)^2}{\Delta} - a^2 \sin^2 \theta \right] \frac{\partial^2 \psi}{\partial t^2} + \frac{4Mar}{\Delta} \frac{\partial^2 \psi}{\partial t \partial \varphi} + \left[ \frac{a^2}{\Delta} - \frac{1}{\sin^2 \theta} \right] \frac{\partial^2 \psi}{\partial \varphi^2} - \Delta^{-s} \frac{\partial}{\partial r} \left( \Delta^{s+1} \frac{\partial \psi}{\partial r} \right) \\ & - \frac{1}{\sin \theta} \frac{\partial}{\partial \theta} \left( \sin \theta \frac{\partial \psi}{\partial \theta} \right) - 2s \left[ \frac{a(r-M)}{\Delta} + \frac{i \cos \theta}{\sin^2 \theta} \right] \frac{\partial \psi}{\partial \varphi} - 2s \left[ \frac{M(r^2 - a^2)}{\Delta} - r - ia \cos \theta \right] \frac{\partial \psi}{\partial t} \\ & + s(s \cot^2 \theta - 1) \psi = 4\pi \Sigma \hat{T} \equiv \mathcal{T}, \end{aligned} \quad (12)$$

where  $s = -2$  is the spin weight corresponding to a gravitational field. The master function  $\psi$  is related to the Weyl scalar by  $\psi = \rho^{-4} \psi_4$ , where  $\psi_4 = -C_{\alpha\beta\gamma\delta} n^\alpha \bar{m}^\beta n^\gamma \bar{m}^\delta$  is the Weyl scalar given by the Newman-Penrose (NP) formalism [94]. The term  $\mathcal{T}$  describes the source of perturbation.

Both the solution  $\psi$  and the source term  $\mathcal{T}$  can be decomposed into multiple modes by variable separation and Fourier transformation, and the result is

$$\psi = \sum_{l=2}^{\infty} \sum_{m=-l}^l \int_{-\infty}^{\infty} d\omega e^{-i\omega t + im\varphi} R_{lm}(r, \omega) \frac{{}_s S_{lm}^{a\omega}(\theta)}{\sqrt{2\pi}}, \quad (13a)$$

$$\mathcal{T} = \sum_{l=2}^{\infty} \sum_{m=-l}^l \int_{-\infty}^{\infty} d\omega e^{-i\omega t + im\varphi} \mathcal{T}_{lm}(r, \omega) \frac{{}_s S_{lm}^{a\omega}(\theta)}{\sqrt{2\pi}}. \quad (13b)$$

Here  ${}_s S_{lm}^{a\omega}(\theta)$  is the spin-weighted spheroidal harmonics (SWSH) function. It satisfies the orthonormalization relation

$$\langle lm | l' m' \rangle \equiv \int_0^\pi {}_s S_{lm}^{a\omega}(\theta) {}_s \bar{S}_{l' m'}^{a\omega}(\theta) \sin \theta d\theta = \frac{\delta_{ll'} \delta_{mm'}}{2\pi}, \quad (14)$$

The function  $R_{lm}(r, \omega)$  is the solution to the radial equation

$$\left[ \Delta^2 \frac{d}{dr} \left( \frac{1}{\Delta} \frac{d}{dr} \right) - \mathcal{V}_{lm}(r, \omega) \right] R_{lm}(r, \omega) = \mathcal{T}_{lm}(r, \omega), \quad (15)$$

where

$$\begin{aligned} \mathcal{V}_{lm}(r, \omega) = & - \frac{K^2 + 4i(r-M)K}{\Delta} \\ & + 8i\omega r + 2ma\omega + \mathcal{A}_{lm} \end{aligned} \quad (16)$$

is the effective potential,  $K = (r^2 + a^2)\omega - ma$ , and  $\mathcal{A}_{lm}$  is the eigenvalue of the SWSH. The homogeneous radial equation allows two independent solutions, and in the so-called ‘‘in-up basis’’ the two solutions have the following asymptotic behavior,

$$R_{lm}^{\text{in}}(r \rightarrow r_+, \omega) = B_{lm}^{\text{tran}} \Delta^2 e^{-ikr^*}, \quad (17a)$$

$$R_{lm}^{\text{in}}(r \rightarrow \infty, \omega) = B_{lm}^{\text{ref}} r^3 e^{i\omega r^*} + \frac{B_{lm}^{\text{inc}}}{r} e^{-i\omega r^*}, \quad (17b)$$

$$R_{lm}^{\text{up}}(r \rightarrow r_+, \omega) = C_{lm}^{\text{inc}} e^{ikr^*} + C_{lm}^{\text{ref}} \Delta^2 e^{-ikr^*}, \quad (17c)$$

$$R_{lm}^{\text{up}}(r \rightarrow \infty, \omega) = C_{lm}^{\text{tran}} r^3 e^{i\omega r^*}, \quad (17d)$$

where  $k = \omega - ma/(2Mr_+)$ ,  $r_\pm = M \pm \sqrt{M^2 - a^2}$  are the roots of  $\Delta = 0$ , and  $r^*$  is the tortoise coordinate defined by

$$\begin{aligned} r^* = & \int \frac{r^2 + a^2}{\Delta} dr, \\ = & r + \frac{2Mr_+}{r_+ - r_-} \ln \frac{r - r_+}{2M} - \frac{2Mr_-}{r_+ - r_-} \ln \frac{r - r_-}{2M}. \end{aligned} \quad (18)$$

The solution to the inhomogeneous radial equation can be constructed from the homogeneous solutions using the Green function method, which results in

$$R_{lm}(r, \omega) = Z_{lm}^{\text{in}}(r, \omega) R_{lm}^{\text{up}}(r, \omega) + Z_{lm}^{\text{up}}(r, \omega) R_{lm}^{\text{in}}(r, \omega). \quad (19)$$

The most challenging and crucial step in our work is calculating the values of  $Z_{lm}^{\text{in}}(r, \omega)$  and  $Z_{lm}^{\text{up}}(r, \omega)$  defined as follows

$$Z_{lm}^{\text{in}}(r, \omega) = \frac{1}{\mathcal{W}_{lm}(\omega)} \int_{r_+}^r dr' \frac{R_{lm}^{\text{in}}(r', \omega)}{\Delta'^2} \mathcal{T}_{lm}(r', \omega), \quad (20a)$$

$$Z_{lm}^{\text{up}}(r, \omega) = \frac{1}{\mathcal{W}_{lm}(\omega)} \int_r^\infty dr' \frac{R_{lm}^{\text{up}}(r', \omega)}{\Delta'^2} \mathcal{T}_{lm}(r', \omega), \quad (20b)$$

where

$$\mathcal{W}_{lm} = 2i\omega C_{lm}^{\text{tran}} B_{lm}^{\text{inc}} \quad (21)$$

is the scaled Wronskian and

$$\begin{aligned} \mathcal{T}_{lm}(r, \omega) = & \mu \int_{-\infty}^\infty dt e^{i\omega t - im\varphi(t)} \Delta^2 \\ & \times \left\{ (A_{nn0} + A_{\bar{m}n0} + A_{\bar{m}\bar{m}0}) \delta[r - r(t)] \right. \\ & + [(A_{\bar{m}n1} + A_{\bar{m}\bar{m}1}) \delta[r - r(t)]],_r \\ & \left. + [A_{\bar{m}\bar{m}2} \delta[r - r(t)]],_{rr} \right\}. \end{aligned} \quad (22)$$

The expressions for  $A_{nn0}$ ,  $A_{\bar{m}n0}$ ,  $A_{\bar{m}\bar{m}0}$ ,  $A_{\bar{m}n1}$ ,  $A_{\bar{m}\bar{m}1}$ , and  $A_{\bar{m}\bar{m}2}$  can be found in Appendix B. Note that here we have assumed the stress-energy of two free monopole particles. We discuss this assumption in further detail in Section V C.

Now we analyze the asymptotic behavior of Eq. (17). When  $r \rightarrow r_+$ , the lower and upper limits in the integration of  $Z_{lm}^{\text{in}}(r, \omega)$  coincide, leading to  $Z_{lm}^{\text{in}}(r, \omega) = 0$ . For the same reason, when  $r \rightarrow \infty$ ,  $Z_{lm}^{\text{up}}(r, \omega) = 0$ . For our b-EMRI, the distance to the source  $r$  is much greater than the size of the system,  $p$ . Therefore, effectively we have  $r/p \rightarrow \infty$ , and in this case the only non-vanishing term is

$$R_{lm}(r \rightarrow \infty, \omega) = Z_{lm}^{\text{in}}(r \rightarrow \infty, \omega) R_{lm}^{\text{up}}(r \rightarrow \infty, \omega). \quad (23)$$

In the following, we will use  $Z_{lm}^{\text{in}}(\omega) \equiv Z_{lm}^{\text{in}}(r \rightarrow \infty, \omega)$ . At infinity, the leading order curvature and metric perturbations are related by

$$\psi_4(r \rightarrow \infty) = \frac{1}{2} \frac{\partial^2}{\partial t^2} (h_+ - ih_\times). \quad (24)$$

Now inserting Eqs. (17), (23), and (24) into Eq. (13), we obtain the Fourier waveform

$$h_+ - ih_\times = -\frac{2}{r} \sum_{lm} \int d\omega \frac{Z_{lm}^{\text{in}}}{\omega^2} \frac{-2S_{lm}^{\omega}(\theta)}{\sqrt{2\pi}} e^{-i\omega(t-r) + im\varphi}. \quad (25)$$

### E. Expansion of the source term

Eq. (10) inspires us to expand the Teukolsky source term into a series in  $d$ . A direct consequence is that the

amplitude  $Z_{lm}^{\text{in}}$  defined in Eq. (20) also becomes a series in  $d$ . To facilitate the expansion of  $Z_{lm}^{\text{in}}$ , we first notice that in the most general case it can be rewritten as

$$Z_{lm}^{\text{in}}(\omega) = \frac{\mu}{\mathcal{W}_{lm}(\omega)} \int_{-\infty}^\infty d\tau \frac{dt}{d\tau} \times e^{i\omega t(\tau, d) - im\varphi(\tau, d)} \mathcal{Z}_{lm}[r(\tau, d), \theta(\tau, d)], \quad (26)$$

where the function  $\mathcal{Z}_{lm}$  inside the integrand is determined by the property of the source, and its exact form is derived in Appendix B. Using Eq. (10), the exponential term is expanded as

$$\begin{aligned} \exp[i\omega t - im\varphi] = & \mathcal{E}_{lm}^{(0)}(\tau, \omega) + \mathcal{E}_{lm}^{(1)}(\tau, \omega) d \\ & + \mathcal{E}_{lm}^{(2)}(\tau, \omega) d^2 + \mathcal{O}(d^3), \end{aligned} \quad (27)$$

where

$$\mathcal{E}_{lm}^{(0)}(\tau, \omega) = \exp[i(\omega u^t - m u^\varphi) \tau], \quad (28a)$$

$$\mathcal{E}_{lm}^{(1)}(\tau, \omega) = \exp[i(\omega u^t - m u^\varphi) \tau] \times i(\omega c_{01} - m c_{31}), \quad (28b)$$

$$\begin{aligned} \mathcal{E}_{lm}^{(2)}(\tau, \omega) = & \exp[i(\omega u^t - m u^\varphi) \tau] \\ & \times \left[ i(\omega c_{02} - m c_{32}) - \frac{1}{2}(\omega c_{01} - m c_{31})^2 \right]. \end{aligned} \quad (28c)$$

We also expand  $\mathcal{Z}_{lm}$  as

$$\begin{aligned} \mathcal{Z}_{lm}[r, \theta] = & \mathcal{Z}_{lm}^{(0)}(r_0, \theta_0) + \mathcal{Z}_{lm}^{(1)}(r_0, \theta_0) d \\ & + \mathcal{Z}_{lm}^{(2)}(r_0, \theta_0) d^2 + \mathcal{O}(d^3), \end{aligned} \quad (29)$$

where

$$\mathcal{Z}_{lm}^{(0)}(r_0, \theta_0) = \mathcal{Z}_{lm}(r, \theta, d) \Big|_{d=0}, \quad (30a)$$

$$\begin{aligned} \mathcal{Z}_{lm}^{(1)}(r_0, \theta_0) = & \frac{d\mathcal{Z}_{lm}(r, \theta, d)}{dd} \Big|_{d=0} \\ = & (\partial_r \mathcal{Z}_{lm})_{d=0} c_{11} + (\partial_\theta \mathcal{Z}_{lm})_{d=0} c_{21} \\ & + (\partial_d \mathcal{Z}_{lm})_{d=0}, \end{aligned} \quad (30b)$$

$$\begin{aligned} \mathcal{Z}_{lm}^{(2)}(r_0, \theta_0) = & \frac{1}{2} \frac{d^2 \mathcal{Z}_{lm}(r, \theta, d)}{dd^2} \Big|_{d=0} \\ = & \frac{1}{2} (\partial_r^2 \mathcal{Z}_{lm})_{d=0} c_{11}^2 + \frac{1}{2} (\partial_\theta \partial_r \mathcal{Z}_{lm})_{d=0} c_{11} c_{21} \\ & + \frac{1}{2} (\partial_d \partial_r \mathcal{Z}_{lm})_{d=0} c_{11} + (\partial_r \mathcal{Z}_{lm})_{d=0} c_{12} \\ & + \frac{1}{2} (\partial_\theta^2 \mathcal{Z}_{lm})_{d=0} c_{21}^2 + \frac{1}{2} (\partial_r \partial_\theta \mathcal{Z}_{lm})_{d=0} c_{21} c_{11} \\ & + \frac{1}{2} (\partial_d \partial_\theta \mathcal{Z}_{lm})_{d=0} c_{21} + (\partial_\theta \mathcal{Z}_{lm})_{d=0} c_{22} \\ & + \frac{1}{2} (\partial_r \partial_d \mathcal{Z}_{lm})_{d=0} c_{11} + \frac{1}{2} (\partial_\theta \partial_d \mathcal{Z}_{lm})_{d=0} c_{21} \\ & + \frac{1}{2} (\partial_d^2 \mathcal{Z}_{lm})_{d=0}. \end{aligned} \quad (30c)$$

By inserting Eqs. (27) and (29) into Eq. (26) and expanding the result into a series of  $d$ , we obtain

$$Z_{lm}^{\text{in}}(\omega) = \frac{\mu}{\mathcal{W}_{lm}(\omega)} \int_{-\infty}^{\infty} \left[ Z_{lm}^{(0)}(\tau, \omega) + Z_{lm}^{(1)}(\tau, \omega)d + Z_{lm}^{(2)}(\tau, \omega)d^2 + \mathcal{O}(d^3) \right] d\tau \quad (31)$$

where

$$Z_{lm}^{(0)}(\tau, \omega) = \mathcal{E}_{lm}^{(0)}(\tau, \omega) \mathcal{Z}_{lm}^{(0)}(r_0, \theta_0), \quad (32a)$$

$$Z_{lm}^{(1)}(\tau, \omega) = \mathcal{E}_{lm}^{(0)}(\tau, \omega) \mathcal{Z}_{lm}^{(1)}(r_0, \theta_0) + \mathcal{E}_{lm}^{(1)}(\tau, \omega) \mathcal{Z}_{lm}^{(0)}(r_0, \theta_0), \quad (32b)$$

$$Z_{lm}^{(2)}(\tau, \omega) = \mathcal{E}_{lm}^{(0)}(\tau, \omega) \mathcal{Z}_{lm}^{(2)}(r_0, \theta_0) + \mathcal{E}_{lm}^{(1)}(\tau, \omega) \mathcal{Z}_{lm}^{(1)}(r_0, \theta_0) + \mathcal{E}_{lm}^{(2)}(\tau, \omega) \mathcal{Z}_{lm}^{(0)}(r_0, \theta_0). \quad (32c)$$

Here, we evaluate  $r$  and  $\theta$  at the CM ( $d = 0$ ) of the IB which, as mentioned before, follows approximately a geodesic circular motion. Hence, we have  $r_0 = p$  and  $\theta_0 = \pi/2$ .

For the zeroth order expansion, the integration is straightforward

$$\begin{aligned} Z_{lm}^{\text{in}(0)}(\omega) &= \frac{\mu}{\mathcal{W}_{lm}(\omega)} \int_{-\infty}^{\infty} Z_{lm}^{(0)}(\omega) d\tau \\ &= \frac{\mu}{\mathcal{W}_{lm}(\omega)} \int_{-\infty}^{\infty} e^{i(\omega u^t - m u^\varphi)\tau} \mathcal{Z}_{lm}^{(0)}(r_0, \theta_0, \omega) d\tau \\ &= \frac{2\pi\mu}{u^t \mathcal{W}_{lm}(\omega)} \delta\left(\omega - m \frac{u^\varphi}{u^t}\right) \mathcal{Z}_{lm}^{(0)}(r_0, \theta_0, \omega) \\ &= \frac{2\pi\mu}{u^t \mathcal{W}_{lm}(\omega_m^{(0)})} \mathcal{Z}_{lm}^{(0)}(r_0, \theta_0, \omega_m^{(0)}). \end{aligned} \quad (33)$$

It reveals that the frequencies corresponding to the zeroth order gravitational radiation are

$$\omega_m^{(0)} = m \frac{u^\varphi}{u^t}, \quad m = -l, \dots, l. \quad (34)$$

Now we turn to the first and second order terms defined in Eqs. (31) and (32). In fact, the presence of the expansion coefficients  $c_{01}, c_{02}, c_{11}, c_{12}, c_{21}, c_{22}, c_{31}, c_{32}$  introduces extra trigonometric terms with respect to  $\tau$ . We use

$$\sin A = \frac{e^{iA} - e^{-iA}}{2i}, \quad \cos A = \frac{e^{iA} + e^{-iA}}{2}, \quad (35)$$

to turn these trigonometric terms into exponential forms. Then by transforming the integration into delta functions as is exemplified in Eq. (33), we obtain the frequencies and amplitudes of the first and second order waveforms.

For the first-order waveform, we find that the frequencies satisfy the condition

$$\omega_{m w v}^{(1)} = m \frac{u^\varphi}{u^t} + w \frac{\Omega}{u^t} + v \frac{\omega_{IB}}{u^t}, \quad (36)$$

where  $m = -l, \dots, l$ ,  $w = 0, \pm 1$ , and  $v = \pm 1$ . Therefore, we have six split first-order modes for each  $m$ . The corresponding amplitudes are

$$Z_{lm}^{\text{in}(1)} = \frac{2\pi\mu}{u^t} \sum_{wv} \frac{Z_{lm w v}^{(1)}}{\mathcal{W}_{lm w v}}. \quad (37)$$

where  $Z_{lm w v}^{(1)} \equiv Z_{lm}^{(1)}(r_0, \theta_0, \omega_{m w v}^{(1)})$  is the split first-order amplitude and  $\mathcal{W}_{lm w v} \equiv \mathcal{W}_{lm}(\omega_{m w v})$  is the Wronskian.

For the second-order waveform, there are fifteen modes for each  $m$ , which are given by

$$\omega_{m w v}^{(2)} = m \frac{u^\varphi}{u^t} + w \frac{\Omega}{u^t} + v \frac{\omega_{IB}}{u^t}, \quad (38)$$

where  $m = -l, \dots, l$ ,  $w = 0, \pm 1, \pm 2$ , and  $v = 0, \pm 2$ . The amplitudes are

$$Z_{lm}^{\text{in}(2)} = \frac{2\pi\mu}{u^t} \sum_{wv} \frac{Z_{lm w v}^{(2)}}{\mathcal{W}_{lm w v}}. \quad (39)$$

where  $Z_{lm w v}^{(2)} \equiv Z_{lm}^{(2)}(r_0, \theta_0, \omega_{m w v}^{(2)})$  is the split second order amplitude. The analytical expressions for the six  $Z_{lm}^{(1)}$  and fifteen  $Z_{lm w v}^{(2)}$  are derived in Appendix C.

## F. Waveform snapshot

Given the above frequency spectra and split amplitudes, Eq. (25) can be expressed as a summation of discrete modes, and the resulting waveform for one small black hole becomes

$$\begin{aligned} h_+ - ih_\times &= -\frac{\mu}{r} \sum_{lm w v} \frac{S_{lm w v}(\theta)}{\omega_{m w v}^2} \\ &\times \left( Z_{lm}^{(0)} + Z_{lm w v}^{(1)} d + Z_{lm w v}^{(2)} d^2 \right) \\ &\times e^{-i\omega_{m w v}(t-r) + im\varphi}, \end{aligned} \quad (40)$$

where  $S_{lm w v}(\theta) \equiv -{}_2S_{lm}^{\omega_{m w v}}(\theta)$ . For the other small black hole, the waveform can be obtained by changing the sign of  $d$ , since we assume equal mass for the two small BHs and use Eq. (6) to describe their inner orbital motion.

Summing up the two waveforms of the two small BHs, we derive the total waveform as

$$\begin{aligned} h_+ - ih_\times &= -\frac{2\mu}{r} \sum_{lm w v} \frac{S_{lm w v}(\theta)}{\omega_{m w v}^2} \\ &\times \left( Z_{lm}^{(0)} + Z_{lm w v}^{(2)} d^2 + \mathcal{O}(d^4) \right) \\ &\times e^{-i\omega_{m w v}(t-r) + im\varphi}, \end{aligned} \quad (41)$$

where all odd-order terms cancel out due to our assumption of a circular, equal-mass IB. However, what we have derived so far is an ideal waveform snapshot, which means that the orbital parameters of the b-EMRI are not evolving. For instance, the outer radius  $p$  remains constant. If

we consider GW radiation, as we will discuss in the next subsection, the orbital parameters will evolve, resulting in a deviation of the waveform phase from the ideal one on a timescale of  $M/\sqrt{\epsilon}$  [6].

### G. Adiabatic evolution of the system

Since GWs carry away energy and angular momentum, the b-EMRI parameters evolve. At leading order in the multi-scale expansion, the evolution can be treated as ‘adiabatic’, in which the local rate of change in the leading order orbital binding energy/angular momentum balances with the leading total asymptotic gravitational wave energy/angular momentum fluxes. While we have highlighted that the b-EMRI correction scales as a 1PA term, its contribution to the inspiral evolution may be incorporated as a sub-leading correction to the adiabatic evolution formula. This is analogous to the inclusion of the secondary’s spin in standard EMRI waveforms.

To calculate the energy and angular momentum carried away by GW, one can start from the effective stress-energy tensor of GW. In the TT gauge it can be written as

$$T_{\alpha\beta}^{GW} = \frac{1}{32\pi} \left\langle \frac{\partial h_{TT}^{ij}}{\partial x^\alpha} \frac{\partial h_{ij}^{TT}}{\partial x^\beta} \right\rangle. \quad (42)$$

Integrating the 03 component over the solid angle yields the average energy fluxes at infinity and at the event horizon  $r_+$ . They can be expressed as

$$\left\langle \frac{d\mathcal{E}}{dt} \right\rangle^\infty = \sum_{lmvw} \frac{1}{4\pi\omega_{mvw}^2} |Z_{lmvw}^{\text{in}}|^2, \quad (43a)$$

$$\left\langle \frac{d\mathcal{E}}{dt} \right\rangle^H = \sum_{lmvw} \frac{1}{4\pi\omega_{mvw}^2} \alpha_{lmvw} |Z_{lmvw}^{\text{up}}|^2. \quad (43b)$$

The angular momentum fluxes are given by

$$\left\langle \frac{d\mathcal{L}_z}{dt} \right\rangle^\infty = \sum_{lmvw} \frac{m}{4\pi\omega_{mvw}^3} |Z_{lmvw}^{\text{in}}|^2, \quad (44a)$$

$$\left\langle \frac{d\mathcal{L}_z}{dt} \right\rangle^H = \sum_{lmvw} \frac{m}{4\pi\omega_{mvw}^3} \alpha_{lmvw} |Z_{lmvw}^{\text{up}}|^2, \quad (44b)$$

where the coefficient  $\alpha_{lmvw}$  is

$$\alpha_{lmvw} = \frac{256(2Mr_+)^5 k(k^2 + 4\kappa^2)(k^2 + 16\kappa^2)\omega_{mvw}^3}{|C_{lmvw}|^2}, \quad (45)$$

with  $k = \omega_{mvw} - ma/(2Mr_+)$ ,  $\kappa = \sqrt{M^2 - a^2}/4Mr_+$ , and

$$\begin{aligned} |C_{lmvw}|^2 &= [(\lambda_{lmvw} + 2)^2 + 4a\omega_{mvw} - 4a^2\omega_{mvw}^2] \\ &\times (\lambda_{lmvw}^2 + 36ma\omega_{mvw} - 36a^2\omega_{mvw}^2) \\ &+ (2\lambda_{lmvw} + 3)(96a^2\omega_{mvw}^2 - 48ma\omega_{mvw}) \\ &+ 144\omega_{mvw}^2(M^2 - a^2), \end{aligned} \quad (46)$$

where  $\lambda_{lmvw} = \mathcal{A}_{lmvw} - 2am\omega_{mvw} + a^2\omega_{mvw}^2 - 2$  with  $\mathcal{A}_{lmvw}$  denoting the eigenvalue of SWSH [95].

The conservation of energy and angular momentum requires that

$$\dot{\mathcal{E}} \equiv \left\langle \frac{d\mathcal{E}}{dt} \right\rangle = - \left\langle \frac{d\mathcal{E}}{dt} \right\rangle^H - \left\langle \frac{d\mathcal{E}}{dt} \right\rangle^\infty, \quad (47a)$$

$$\dot{\mathcal{L}}_z \equiv \left\langle \frac{d\mathcal{L}_z}{dt} \right\rangle = - \left\langle \frac{d\mathcal{L}_z}{dt} \right\rangle^H - \left\langle \frac{d\mathcal{L}_z}{dt} \right\rangle^\infty. \quad (47b)$$

If we treat the inspiral process as an ‘osculating’ slide through a series of geodesics, the above  $\dot{\mathcal{E}}$  and  $\dot{\mathcal{L}}_z$  determine how the system evolves from one geodesic to the next. In the circular-equatorial case, the geodesic parameters are  $M$ ,  $a$ ,  $p$ . The evolution of mass and spin of the SMBH formally appears at 1PA order in the multi-scale expansion though it is known to be numerically subdominant (see e.g. Ref. [19]). The only parameter we need to evolve is the outer radius  $p$ . Now that the energy  $\mathcal{E}(t)$  and angular momentum  $\mathcal{L}_z(t)$  at each moment are known, we can derive

$$\dot{p} \equiv \frac{dp}{dt} = q_1 \dot{\mathcal{E}} + q_2 \dot{\mathcal{L}}_z, \quad (48)$$

where  $q_1$  and  $q_2$  are functions of  $\mathcal{E}$ ,  $\mathcal{L}_z$  and  $p$ , and these two functions are derived as follows. Since circular orbit remains circular during radiation reaction [96–99], we have  $\dot{R} = 0$  and  $\dot{R}' = 0$  according to the radial geodesic equation defined in Eq. (5). The former equation relates the energy and angular-momentum fluxes to the properties of the circular-equatorial orbits, which is

$$\frac{\dot{\mathcal{E}}}{\dot{\mathcal{L}}_z} = \frac{M^{1/2}}{aM^{1/2} + p^{3/2}} = \frac{u^\varphi}{u^t}. \quad (49)$$

The latter gives the expressions for  $q_1$  and  $q_2$  as

$$q_1 = - \frac{2[2\mathcal{E}p^3 - aM\mathcal{L}_z + a^2\mathcal{E}(M+p)]}{a^2(\mathcal{E}^2 - 1) - \mathcal{L}_z^2 + 6p[M + (\mathcal{E}^2 - 1)p]}, \quad (50a)$$

$$q_2 = - \frac{2[\mathcal{L}_z(M-p) - aM\mathcal{E}]}{a^2(\mathcal{E}^2 - 1) - \mathcal{L}_z^2 + 6p[M + (\mathcal{E}^2 - 1)p]}. \quad (50b)$$

Now we have the evolution of  $p = p(t)$ , we can compute the adiabatic waveform as

$$h_+ - ih_\times = \frac{\mu}{r} \sum_{lm} H_{lm}(t, \theta, \varphi) e^{-i\Phi_m(t)}, \quad (51)$$

where

$$H_{lm}(t, \theta, \varphi) = - \frac{2S_{lm}(t, \theta)}{(\omega_m(t))^2} Z_{lm}^{(0)}(t) e^{im\varphi}, \quad (52a)$$

$$\Phi_m(t) = \int_0^t \omega_m(t') dt'. \quad (52b)$$

Here all terms containing  $p$  become a function of  $t$ . The phase term is accumulative so it is an integral. Note that above we only include zeroth order modes in adiabatic waveforms to illustrate the main features.



### III. NUMERICAL IMPLEMENTATION

#### A. Frequencies and amplitudes of the modes

Our waveform model reveals three key frequencies:

$$\Omega_G \equiv \frac{u^\varphi}{u^t}, \quad \Omega_P \equiv \frac{\Omega}{u^t}, \quad \Omega_I \equiv \frac{\omega_{IB}}{u^t}. \quad (53)$$

In particular, the geodesic frequency  $\Omega_G$  and precession frequency  $\Omega_P$  have similar magnitudes, whereas the rescaled inner frequency  $\Omega_I$  is significantly higher than the previous two. For instance, when the parameters are  $a = 0.9M$ ,  $p = 10M$ ,  $\epsilon = 10^{-5}$ , and  $d = 4000\mu$ , we have  $\Omega_G = 0.0307/M$ ,  $\Omega_P = -0.0268/M$ , and  $\Omega_I = 0.3344/M$ .

The frequency spectrum given by Eqs. (34), (36) and (38) takes the general form

$$\omega_{m\ell v} = m\Omega_G + w\Omega_P + v\Omega_I. \quad (54)$$

Notice that for the second order modes with  $v = \pm 2$ , the frequency can reach values as high as  $\omega \sim \mathcal{O}(1/M)$ . In this high-frequency regime, it becomes challenging to compute the homogeneous Teukolsky radial solutions  $R_{lm}^{\text{in/up}}$  using the conventional MST method [88, 100–102].

To address the problems posed by the high frequencies, we use the Sasaki-Nakamura (SN) method instead [103], which offers smoother and faster performance in this high-frequency regime. A detailed presentation of the SN method, along with the Julia package `GeneralizedSasakiNakamura.jl` used for computing  $R_{lm}^{\text{in/up}}$  can be found in Ref. [104]. Additionally, we employ the `SpinWeightedSpheroidalHarmonics.jl` package to compute the SWSH and their eigenvalues. With these ingredients in place, the amplitudes  $Z_{lm}^{(0)}$ ,  $Z_{lmwv}^{(1)}$ , and  $Z_{lmwv}^{(2)}$  can be calculated according to the algorithm outlined in Appendix C.

#### B. Waveform and truncation

When calculating the waveform according to Eq. (41), in principle an infinite number of modes are needed. In practice, the  $l = 2$  modes already capture the main features of the waveform. Including higher  $l$  modes does improve precision, but the fractional error falls below  $10^{-6}$  when we truncate the modes at  $l_{\text{max}} = 10$ , and below  $10^{-11}$  when  $l_{\text{max}} = 15$ . To save computational time, in this work we truncate the modes at  $l_{\text{max}} = 10$  when computing the flux (also see [17]) and at  $l_{\text{max}} = 5$  when plotting the waveforms.

To evolve the outer orbit, we select a set of grids starting from  $p_{\text{init}} = 10.0M$  to a value close to the innermost stable circular orbit (ISCO) [105]. When  $a = 0.9M$ , ISCO is located at about  $p = 2.32M$ . We stop at  $p_{\text{final}} = 2.35M$ , as the system transits rapidly from inspiral to plunge near the ISCO. The grid spacing is chosen

according to

$$\Delta p(/M) = 0.05 \tanh(p - p_{\text{final}}) + 0.001. \quad (55)$$

This results in 214 grid points between  $p_{\text{init}} = 10.0M$  and  $p_{\text{final}} = 2.35M$ .

At each grid point, we compute the energy and angular momentum fluxes  $\dot{\mathcal{E}}(p)$  and  $\dot{\mathcal{L}}_z(p)$ . Using Eq. (48) we obtain  $\dot{p}$  at these grids. Cubic spline interpolation [106] is used off the grid points to compute  $\dot{p}(p)$  in the inspiraling regime  $p \in [p_{\text{final}}, p_{\text{init}}]$ . Then we numerically integrate Eq. (48) to recover the evolution of  $p$  with respect to  $t$ . By inserting  $p(t)$  into Eqs. (51) and (52) we obtain the adiabatic waveform. Note that we exclude modes with  $\omega_{m\ell v} < \Omega_G + \Omega_P$  to avoid the so-called transient resonance, as discussed in Ref. [107, 108].

### IV. RESULTS

#### A. Amplitude, Flux, and resonant excitation of QNMs

From the analysis in the previous section, the first order amplitudes cancel, leaving us with

$$\begin{aligned} Z_{lmwv}^{\text{in}} &= Z_{lm}^{(0)} + Z_{lmwv}^{(2)} d^2 \\ &= \begin{cases} Z_{lm}^{(0)} + Z_{lm00}^{(2)} d^2 & w = v = 0, \\ Z_{lmwv}^{(2)} d^2 & \text{others.} \end{cases} \end{aligned} \quad (56)$$

For  $w = v = 0$ , the fluxes are proportional to

$$\begin{aligned} |Z_{lm00}^{\text{in}}|^2 &= \left| Z_{lm}^{(0)} \right|^2 + \left( Z_{lm}^{(0)} \bar{Z}_{lm00}^{(2)} + \bar{Z}_{lm}^{(0)} Z_{lm00}^{(2)} \right) d^2 \\ &\quad + \left| Z_{lm00}^{(2)} \right|^2 d^4, \end{aligned} \quad (57)$$

while for  $w \neq 0$  or  $v \neq 0$

$$\left| Z_{lmwv}^{\text{in}} \right|^2 = \left| Z_{lmwv}^{(2)} \right|^2 d^4. \quad (58)$$

We first consider the modes with  $v = 0$ . In this case, the leading-order correction to the amplitude is of the order of  $\sim \mathcal{O}(d^2)$ . We define a factor

$$A_{lmwv}(\omega) = \frac{|Z_{lmwv}^{(2)}| d^2}{|Z_{lm}^{(0)}|} \quad (59)$$

to quantify the relative importance of this correction. Table II shows the amplitudes of the main modes and the corresponding leading-order corrections when  $v = 0$ . We can draw the conclusion that  $A_{lm00} \sim \epsilon$ . To understand this relation, we note that although the corrections are proportional to  $d^2$ , the inner diameter  $d$  is of the order of thousands of  $\mu$ . Therefore, we have  $d^2 = (\text{thousands of } M\epsilon)^2 \approx M^2\epsilon$ .

When  $v = \pm 2$  (high-frequency modes), the factors are much larger, especially when the frequency approaches

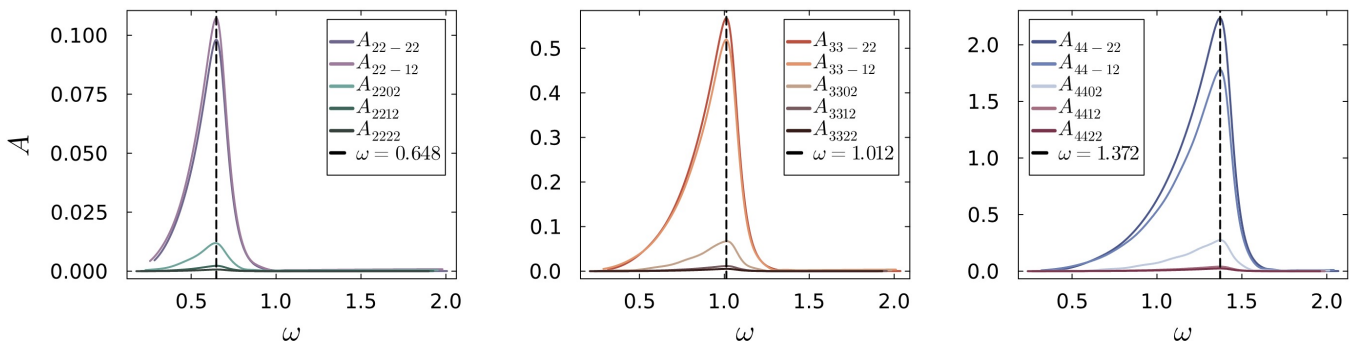


FIG. 3: The factors  $A_{22w2}$ ,  $A_{33w2}$ , and  $A_{44w2}$  with  $w = 0, \pm 1, \pm 2$  as functions of the frequency  $\omega$ . Peaks appear at  $\omega = 0.648/M$  for  $l = m = 2$  modes, at  $\omega = 1.012/M$  for  $l = m = 3$  modes, and at  $\omega = 1.372/M$  for  $l = m = 4$  modes.

l	m	$ Z_{lm}^{(0)} $	$ Z_{lm00}^{(2)}  \cdot d^2$	$A_{lm00}$
2	2	$1.03 \times 10^{-3}$	$3.74 \times 10^{-8}$	$3.63 \times 10^{-5}$
3	3	$5.19 \times 10^{-4}$	$2.32 \times 10^{-8}$	$4.47 \times 10^{-5}$
4	4	$2.59 \times 10^{-4}$	$1.40 \times 10^{-8}$	$5.40 \times 10^{-5}$
5	5	$1.26 \times 10^{-4}$	$8.05 \times 10^{-8}$	$6.40 \times 10^{-5}$
6	6	$5.95 \times 10^{-5}$	$4.44 \times 10^{-9}$	$7.45 \times 10^{-5}$
7	7	$2.76 \times 10^{-5}$	$2.36 \times 10^{-9}$	$8.53 \times 10^{-5}$
8	8	$1.26 \times 10^{-5}$	$1.22 \times 10^{-9}$	$9.64 \times 10^{-5}$

TABLE II: The zeroth and second order amplitudes and their fractions of main modes, with parameters  $a = 0.9M$ ,  $p = 10M$ ,  $\epsilon = 10^{-5}$ ,  $d = 4000\mu$ ,  $\tilde{\psi} = \pi/4$ , and  $\tilde{\theta} = \pi/3$ .

the QNM frequencies of the SMBH. Fig. 3 illustrates the dependence of  $A_{lmwv}$  on the frequency  $\omega$ . The parameters are the same as in Table. II. Peaks are observed near the corresponding QNM modes. The corresponding frequencies of the peaks are given in Table III. We also give the frequencies of the QNMs for comparison, which are calculated using the Python package `qnm.py` [109]. Notably, the peaks occur slightly below the real part of the leading QNM frequencies. These features agree well with Fig. 2 of Ref. [63], where this behavior is interpreted as a resonant excitation of QNMs.

l	m	$\omega_{lm0}^{\text{QNM}}(M)$	$\omega_{lm}^{\text{peak}}(M)$
2	2	$0.672-0.0649i$	0.648
3	3	$1.045-0.0655i$	1.012
4	4	$1.410-0.0662i$	1.372

TABLE III: QNM frequencies of the leading tones and peak frequencies of the  $l = m = 2, 3, 4$  modes.

It is remarkable that the ratios  $A_{lmwv}$  for the high-frequency modes with  $v = \pm 2$  can approach unity in some cases. These relative second-order amplitudes are about  $\epsilon^{-1}$  times larger than those of the low-frequency modes. Moreover, for each  $m$ , there are ten high-frequency modes corresponding to  $w = 0, \pm 1, \pm 2$ ,  $v = \pm 2$ . Therefore,

the fluxes are amplified by another order of magnitude. Such a large flux due to the high-frequency modes should cause the b-EMRI system to evolve faster than a standard EMRI. We notice that an earlier study using the MPD equation to solve the evolution of b-EMRI also revealed the appearance of two high-frequency modes (see Eq. (30) in Ref. [65]). However, the authors disregarded these two terms in the calculation of the flux, which potentially could result in a slower evolution of their b-EMRI.

To better see the importance of the high-frequency modes, we calculate the energy fluxes due to different modes,

$$\dot{\mathcal{E}}^{\infty(0)} = \sum_{l=2}^{10} \sum_{m=-l}^l \frac{1}{4\pi\omega_m^2} \left| Z_{lm}^{(0)} \right|^2, \quad (60a)$$

$$\dot{\mathcal{E}}^{\infty(1)} = \sum_{l=2}^{10} \sum_{m=-l}^l \frac{1}{4\pi\omega_m^2} \left| Z_{lm}^{(0)} + Z_{lm00}^{(2)} d^2 \right|^2, \quad (60b)$$

$$\dot{\mathcal{E}}^{\infty(2)} = \sum_{l=2}^{10} \sum_{m=vw} \frac{1}{4\pi\omega_{m=vw}^2} \left| Z_{lm}^{(0)} + Z_{lmwv}^{(2)} d^2 \right|^2, \quad (60c)$$

where we have truncated the calculation at  $l_{\text{max}} = 10$ . Here,  $\dot{\mathcal{E}}^{\infty(0)}$  represents the energy flux of a standard EMRI,  $\dot{\mathcal{E}}^{\infty(1)}$  accounts for low-frequency corrections similar to those discussed in Ref. [65], and  $\dot{\mathcal{E}}^{\infty(2)}$  includes the contributions from high-frequency modes. The energy fluxes down to the horizon  $\dot{\mathcal{E}}^{H(0)}$ ,  $\dot{\mathcal{E}}^{H(1)}$ ,  $\dot{\mathcal{E}}^{H(2)}$  are also computed, and all the results are given in Table IV.

From the table we find that that the contributions from the b-EMRI high-frequency modes are substantial, particularly during the early inspiral stage. This leads to a faster evolution of the b-EMRI system compared to a standard EMRI. In contrast, the low-frequency modes contribute only at the  $\mathcal{O}(\epsilon)$  order. The behavior of the angular momentum fluxes mirrors that of the energy fluxes and hence are not shown here.

Fig. 4 shows more clearly the resonant excitation of the QNMs by the high-frequency modes of the b-EMRI. Here we choose  $\epsilon = 10^{-5}$  and use different values of  $d$  to change the total frequency  $\omega$ . Therefore,  $d = 8000\mu$  corresponds

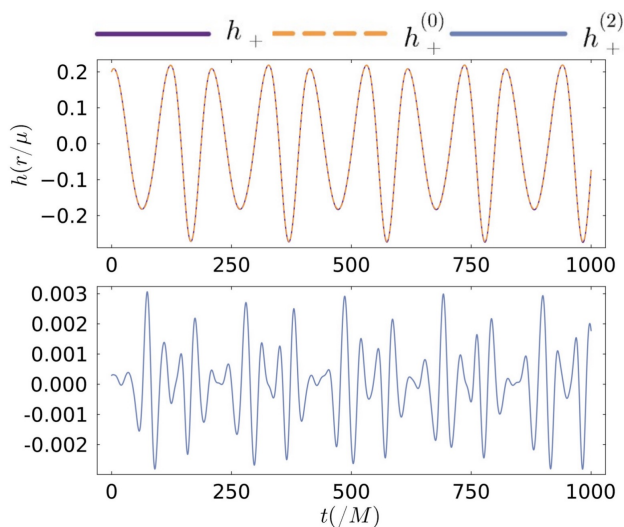
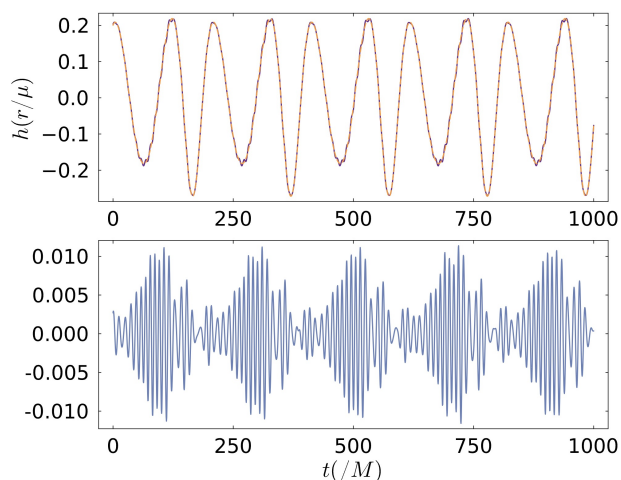
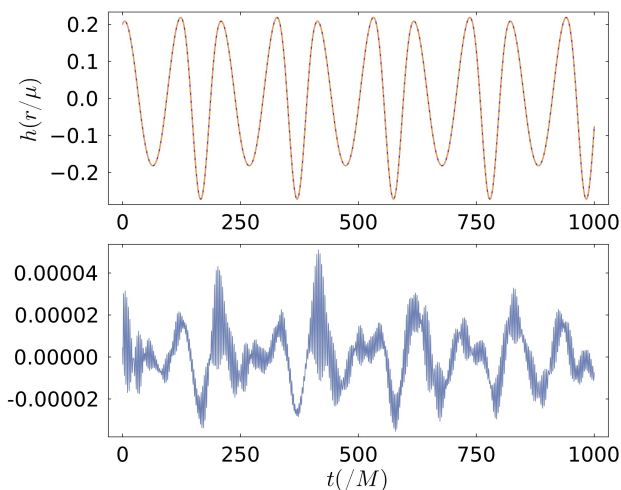
(a) Low-frequency inner motion with  $d = 8000\mu$ (b) Inband-frequency inner motion with  $d = 4000\mu$ (c) High-frequency inner motion with  $d = 2000\mu$ 

FIG. 4: Waveform snapshots with different setting of  $d$ . Other parameters are fixed at  $a = 0.9M$ ,  $p = 10M$ ,  $\epsilon = 10^{-5}$ ,  $\tilde{\psi} = \pi/4$ ,  $\tilde{\theta} = \pi/3$  with viewing angles  $\theta = \pi/3$  and  $\varphi = \pi/6$ .

to a low frequency of  $2\Omega_I = 0.236/M$ ,  $d = 4000\mu$  corresponds to an in-band frequency of  $2\Omega_I = 0.669/M$ , and  $d = 2000\mu$  corresponds to a high frequency of  $2\Omega_I = 1.892/M$ . The term “in-band” means that the frequency lies within the band that resonantly excites the QNMs. From Fig. 3 and Table. III, it is clear that the frequencies associated with  $d = 4000\mu$  center around the excitation band of the  $l = m = 2$  QNM.

When the frequency is within the excitation band, we find that the second-order amplitude  $h_+^{(2)}$  is significantly excited, reaching about 10% of that of  $h_+^{(0)}$ , which results in a visible fluctuation in the composite waveform  $h_+$  in panel (b) of Fig. 4. Conversely, when the frequency is outside the excitation band (either lower or higher), the QNMs are not excited, and the amplitude of  $h_+^{(2)}$  is relatively small. It is also worth noting that  $h_+^{(2)}$  in panel (a) of Fig. 4 is larger than that in panel (c). This is because, as  $d$  increases, the  $\mathcal{O}(d^2)$  factor also increases.

## B. Adiabatic trajectory and waveform

In this subsection, we study the adiabatic evolution of the b-EMRI system with different configurations and compare it with a standard EMRI. We continue to use the parameters  $a = 0.9M$ ,  $p = 10M$ ,  $\epsilon = 10^{-5}$ ,  $d = 4000\mu$ ,  $\tilde{\psi} = \pi/4$ , and  $\tilde{\theta} = \pi/3$ . We also adopt the configurations defined in Eq. (60). Eq. (60a) corresponds to the evolution of a standard EMRI. Eq. (60b) represents the evolution of a b-EMRI driven only by the low-frequency modes, and we refer to this case as “Configuration 1”. Eq. (60c) includes all modes, which we refer to as “Configuration 2”.

Fig. 5 shows the evolution of the parameter  $p$ . With our choice of parameters, it takes 69% of the evolution time of the EMRI for the b-EMRI system to evolve from  $p_{\text{init}} = 10M$  to  $p_{\text{final}} = 2.35M$  if we account for high-frequency modes. During the early inspiral stage, the b-EMRI system under “Configuration 2” evolves significantly faster than both the standard EMRI and the b-EMRI with “Configuration 1”. For example, if we take  $M = 10^6 M_\odot$ , the inspiral timescale for an EMRI in our fiducial model is 3.9 years and is 2.7 years for a b-EMRI under “Configuration 2”. The difference in the evolution time between the EMRI and the b-EMRI with “Configuration 1” is small, roughly  $1899M \approx 2.6\text{h}$  in this case.

With the trajectory  $p(t)$  in hand, we further compute the adiabatic waveforms for both the EMRI and the b-EMRI systems. Fig. 6 shows the results. When including only the low-frequency modes into the fluxes, the waveforms of the standard EMRI and b-EMRI systems start to deviate in phase after about  $5 \times 10^4$  outer orbital periods. In contrast, when including the high-frequency modes, the deviation in phase already appears only after 40 outer orbital periods.

These results suggest that the high-frequency modes contribute significantly more to the evolution of the b-

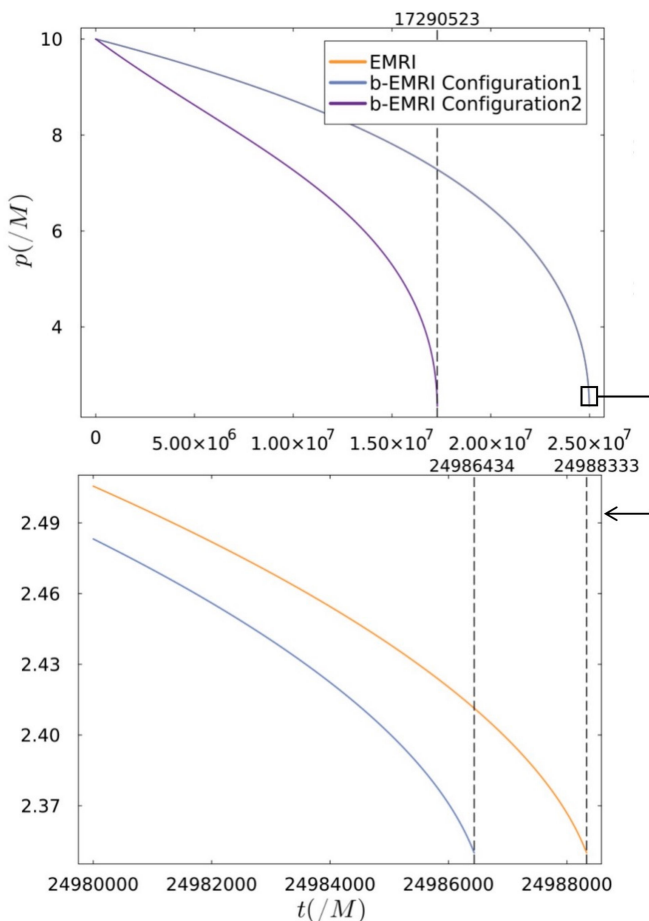


FIG. 5: Evolution of the outer radius  $p$  with three different configurations. The upper panel shows the long-term evolution and the lower one zooms in at the final stage of the system.

EMRI system than the low-frequency modes. As a result, the b-EMRI system evolve much faster than a standard EMRI in the early inspiral phase. This observation extends beyond the current understanding of b-EMRI system evolution. For example, in Fig. 2 of Ref. [65] where the contribution of the high-frequency modes are not included, we see a much slower evolution of the b-EMRI system which is consistent with what we have derived in Fig. 6(a).

We also find that the influence of the high-frequency modes diminishes as the parameter  $p$  decreases due to radiation reaction effects. This is caused probably by the fact that the averaged outer circular orbit starts to produce modes with higher frequencies as  $p$  shrinks. These modes could be as strong as the modes produced by the  $d^2$  terms of the b-EMRI. As a result, a key feature of the b-EMRI waveform is its faster evolution during the early inspiral stage, and the converging to the standard EMRI rate as  $p$  becomes smaller. This characteristic might be used to distinguish b-EMRIs from standard EMRI systems.

## V. DISCUSSION

### A. Comparisons with previous works

Now we compare our results with those presented in three previous works [63, 65, 73]. The first BH perturbation theory based model of b-EMRI waveforms appears in Ref. [63]. Although the source term of the perturbation is simplified and has only one frequency in that study, it already shows that the perturbation can resonantly excite the QNMs of the central SMBH. Moreover, in that study the excitation ratio is defined as

$${}_s\mathcal{R}_{lm} = {}_s\dot{E}_{lm} / {}_s\dot{E}_{Nlm}, \quad (61)$$

so that  ${}_s\mathcal{R}_{lm}$  tracks the flux excited by the high-frequency motion of the IB. The behavior of this ratio as a function of frequency  $\omega$  is similar to our  $A_{lm\nu\nu}$  defined in Eq. (43). For example, Fig. 3 in our work agrees with Fig. 2 of Ref. [63]. Both figures show that the positions of the peaks  $\omega_{lm}^{\text{peak}}$  are slightly smaller than the real parts of the QNMs frequencies  $\omega_{lm0}^{\text{QNM}}$ , and the curves are flatter on the left of the peaks while steeper on the right.

To better interpret the above results, we need to understand the nature of QNMs. They are solutions to the homogeneous Teukolsky radial equation Eq. (15) satisfying purely outgoing boundary condition at infinity and purely ingoing boundary condition at the horizon. According to these solutions, the asymptotic amplitudes  $B_{lm}^{\text{inc}}$  and  $C_{lm}^{\text{inc}}$  in Eq. (17) go zero when  $\omega = \omega_{lm0}^{\text{QNM}}$ . This will make the Wronskian  $\mathcal{W}_{lm}(\omega)$  vanish and the amplitude  $Z_{lm\nu\nu}^{(2)}$  diverge, as one can see in Eqs. (20) and (21). However,  $\omega_{lm0}^{\text{QNM}}$  is a complex frequency but  $\omega_{m\nu\nu}$ , the frequency associated with the b-EMRI, is a real one. So the system cannot achieve  $B_{lm}^{\text{inc}} = C_{lm}^{\text{inc}} = 0$  even when the real parts of these two frequencies completely match. Such a mismatch results in a finite peak.

Later, Ref. [65] treats the inner binary as a mass distribution and expands it into multipole moments to compute the source term. To evolve the outer orbit, the authors treat the BBH as a single spinning body and use the MPD equation to compute its orbit around the SMBH. This approach ensures conservation of the stress-energy tensor and inspires us to discuss the validity of our model in Sec. V C. However, in their study the authors omitted the high-frequency source terms because the frequencies are outside the LISA band. Our results, nevertheless, shows that these dropped high-frequency modes, if resonate with the central SMBH's QNMs, will enhance energy dissipation.

Notably, the IB is allowed to evolve and merger in Ref. [65], so the b-EMRI will be an important multi-band GW source which can produce both high-frequency GW in the LIGO/Virgo band and low-frequency GW in the LISA band [40]. The merger of the IB also leads to a sudden mass loss making the low-frequency waveform more distinguishable. These potential multi-band observational aspects are not discussed in our work.



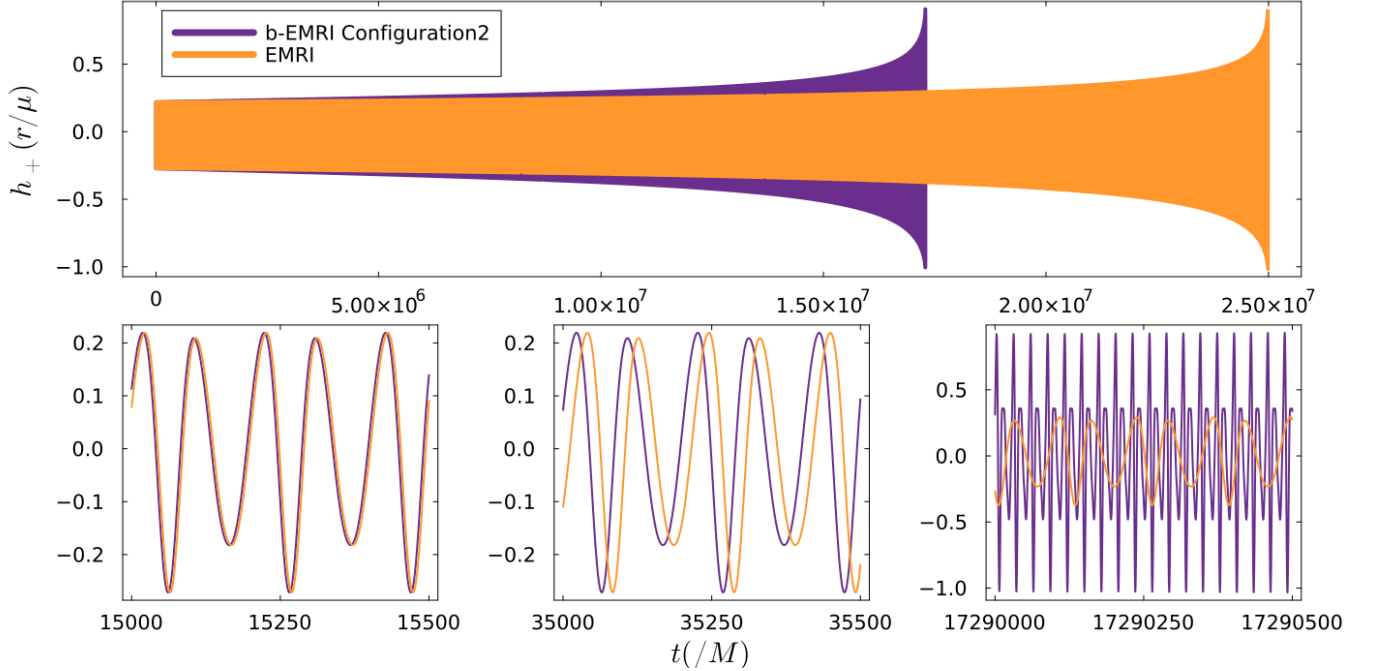
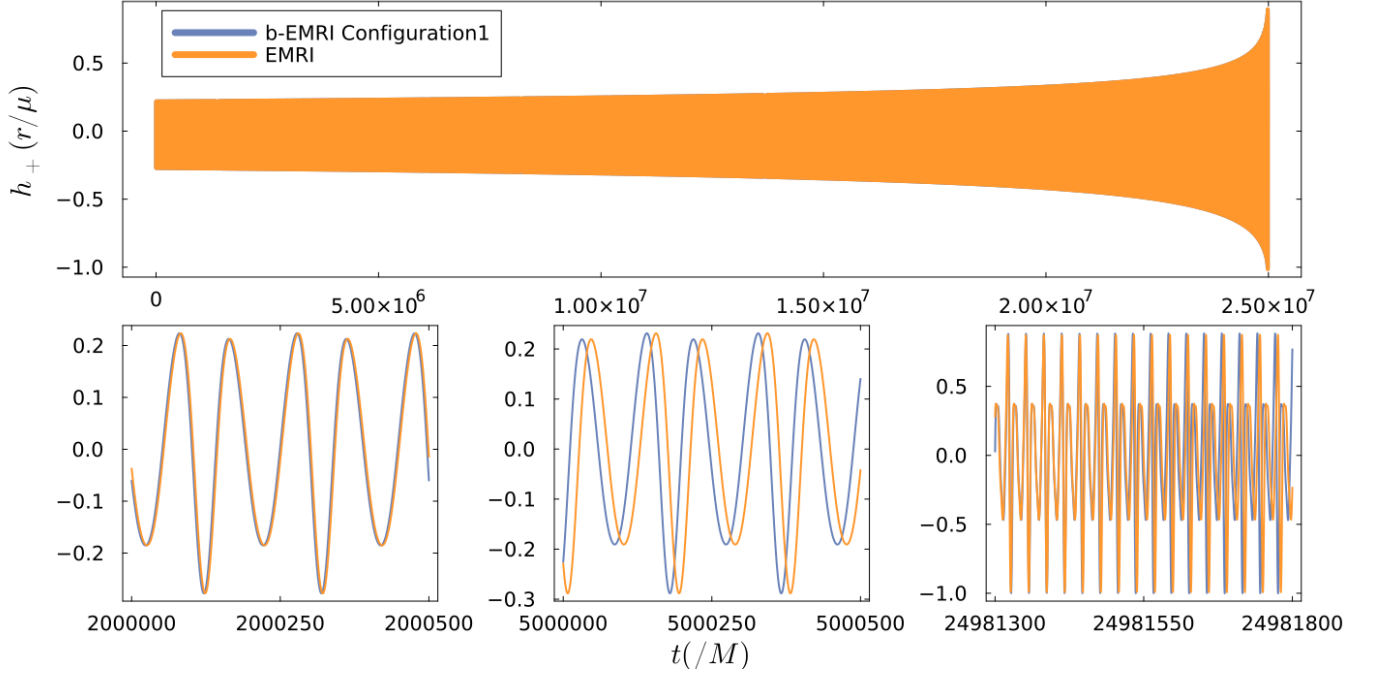


FIG. 6: The upper panels of (a) and (b) show the full adiabatic waveforms of the EMRI (orange curve) and the b-EMRI with different configurations (blue curve and purple curve). The time span covers the evolution from  $p_{\text{init}} = 10M$  to  $p_{\text{final}} = 2.35M$ . The lower three panels of (a) and (b) are chosen to show the how the deviation in phase (dephasing) progresses at the beginning, in the middle and at the end.



$p/M$	$d/\mu$	$\dot{\mathcal{E}}^{\infty(0)}/(\epsilon^2)$	$\dot{\mathcal{E}}^{\infty(1)}/(\epsilon^2)$	$\dot{\mathcal{E}}^{\infty(2)}/(\epsilon^2)$	$\dot{\mathcal{E}}^{H(0)}/(\epsilon^2)$	$\dot{\mathcal{E}}^{H(1)}/(\epsilon^2)$	$\dot{\mathcal{E}}^{H(2)}/(\epsilon^2)$
10	2000	$5.04909 \times 10^{-5}$	$5.04969 \times 10^{-5}$	$1.40386 \times 10^{-4}$	$-1.43895 \times 10^{-6}$	$-1.43910 \times 10^{-6}$	$1.10771 \times 10^{-3}$
10	4000	$5.04909 \times 10^{-5}$	$5.04945 \times 10^{-5}$	$7.01751 \times 10^{-5}$	$-1.43895 \times 10^{-6}$	$-1.43903 \times 10^{-6}$	$2.12752 \times 10^{-5}$
10	6000	$5.04909 \times 10^{-5}$	$5.04937 \times 10^{-5}$	$5.31631 \times 10^{-5}$	$-1.43895 \times 10^{-6}$	$-1.43901 \times 10^{-6}$	$-1.44617 \times 10^{-6}$
10	8000	$5.04909 \times 10^{-5}$	$5.04934 \times 10^{-5}$	$5.08327 \times 10^{-5}$	$-1.43895 \times 10^{-6}$	$-1.43902 \times 10^{-6}$	$-1.44713 \times 10^{-6}$
8	2000	$1.46335 \times 10^{-4}$	$1.46352 \times 10^{-4}$	$1.98487 \times 10^{-4}$	$-7.51153 \times 10^{-6}$	$-7.51229 \times 10^{-6}$	$5.96528 \times 10^{-4}$
8	4000	$1.46335 \times 10^{-4}$	$1.46346 \times 10^{-4}$	$1.58943 \times 10^{-4}$	$-7.51153 \times 10^{-6}$	$-7.51195 \times 10^{-6}$	$2.16421 \times 10^{-6}$
8	6000	$1.46335 \times 10^{-4}$	$1.46344 \times 10^{-4}$	$1.47468 \times 10^{-4}$	$-7.51153 \times 10^{-6}$	$-7.51192 \times 10^{-6}$	$-7.46815 \times 10^{-6}$
8	8000	$1.46335 \times 10^{-4}$	$1.46343 \times 10^{-4}$	$1.46488 \times 10^{-4}$	$-7.51153 \times 10^{-6}$	$-7.51200 \times 10^{-6}$	$-7.51337 \times 10^{-6}$
6	2000	$5.65865 \times 10^{-4}$	$5.65934 \times 10^{-4}$	$5.90544 \times 10^{-4}$	$-6.04253 \times 10^{-5}$	$-6.04311 \times 10^{-5}$	$3.84389 \times 10^{-4}$
6	4000	$5.65865 \times 10^{-4}$	$5.65910 \times 10^{-4}$	$5.71402 \times 10^{-4}$	$-6.04253 \times 10^{-5}$	$-6.04289 \times 10^{-5}$	$-5.81383 \times 10^{-5}$
6	6000	$5.65865 \times 10^{-4}$	$5.65903 \times 10^{-4}$	$5.66266 \times 10^{-4}$	$-6.04253 \times 10^{-5}$	$-6.04294 \times 10^{-5}$	$-6.04366 \times 10^{-5}$
6	8000	$5.65865 \times 10^{-4}$	$5.65900 \times 10^{-4}$	$5.65955 \times 10^{-4}$	$-6.04253 \times 10^{-5}$	$-6.04311 \times 10^{-5}$	$-6.04320 \times 10^{-5}$
4	2000	$3.59721 \times 10^{-3}$	$3.59767 \times 10^{-3}$	$3.60627 \times 10^{-3}$	$-7.76063 \times 10^{-4}$	$-7.76124 \times 10^{-4}$	$-6.75433 \times 10^{-4}$
4	4000	$3.59721 \times 10^{-3}$	$3.59753 \times 10^{-3}$	$3.59869 \times 10^{-3}$	$-7.76063 \times 10^{-4}$	$-7.76120 \times 10^{-4}$	$-7.76084 \times 10^{-4}$
4	6000	$3.59721 \times 10^{-3}$	$3.59746 \times 10^{-3}$	$3.59756 \times 10^{-3}$	$-7.76063 \times 10^{-4}$	$-7.76157 \times 10^{-4}$	$-7.76162 \times 10^{-4}$
4	8000	$3.59721 \times 10^{-3}$	$3.59738 \times 10^{-3}$	$3.59742 \times 10^{-3}$	$-7.76063 \times 10^{-4}$	$-7.76221 \times 10^{-4}$	$-7.76234 \times 10^{-4}$

TABLE IV: Energy fluxes due to different modes when  $a = 0.9M$ ,  $\epsilon = 10^{-5}$ ,  $\tilde{\psi} = \pi/4$ , and  $\tilde{\theta} = \pi/3$

More recently, Ref. [73] uses the ‘‘Numerical Kludge’’ template to generate the waveform of b-EMRI. The OB in that work takes a generic orbit and the IB is eccentric, making the b-EMRI more realistic. However, the trajectories of the small BHs around the SMBH are still derived from an algebraic combination of the inner and outer motion. Therefore, the method cannot fully deal with the relativistic effects on the (three-body) GW source in the strong-gravity regime. Interestingly, the waveform snapshots shown in Ref. [73] also exhibit strong modulation by the existence of the IB. However, this modulation is not associated with the excitation of QNMs, but due to the large inner orbital motion of the two stellar-mass BHs, since the semi-latus rectum of their IB (which is analogous to  $d$  in this work) is a significant fraction of the size of the OB. Such a large IB raises the issue of stability for the three-body system. We will discuss this issue in the next subsection.

### B. Parameter space

Throughout this work, we assume no evolution of the IB, which means that the IB is neither tidally disrupted nor excited to high eccentricities. The stability of a hierarchical three-body system is a classical problem [110]. The maximum distance for the two bodies in the IB to remain stable is determined by the Hill radius,  $R_H := (\epsilon/3)^{1/3}p$ , where Newtonian gravity is assumed. Since here we are working in the strong-gravity regime, we require  $d < R_H/3$ , to be conservative. Given our fiducial model in which  $p = 10M$  and  $\epsilon = 10^{-5}$ , we find  $d < 0.05M$ . In other words, an IB with  $d = 4000\mu = 0.04M$  is stable in this case. Additionally, since we assume Newtonian motion for the inner orbital motion,  $d$  should be sufficiently large to avoid strong relativistic correction. For this latter reason, we

set  $d > 1000\mu = 1000M\epsilon$ .

Another important assumption in this work is that the inner binary follows a circular orbit. However, dynamical effects in triple systems, such as the Kozai-Lidov mechanism [111, 112], could excite the eccentricity of the IB if the inclination angle  $\tilde{\theta}$  between the inner and outer orbits exceeds a critical value. The timescale of the eccentric Kozai-Lidov mechanism (EKM) was derived in Ref. [113, 114], which gives

$$\tau_{\text{EKM}} = \frac{256\sqrt{10}}{15\pi\sqrt{\epsilon_{\text{oct}}}} t_{\text{sec}}, \quad (62)$$

where

$$t_{\text{sec}} = \frac{\sqrt{M_C d}}{\Phi_0}, \quad (63a)$$

$$\epsilon_{\text{oct}} = \frac{d}{p} \frac{e}{1 - e^2}, \quad (63b)$$

$$\Phi_0 = \frac{M d^2}{p^3(1 - e^2)^{3/2}}, \quad (63c)$$

$M_C = \mu/4$  is the reduced mass of the IB, and  $e$  is an eccentricity parameter of the OB. If we assume a circular outer orbit but allow a small eccentricity  $e \ll 1$  to study the EKM timescale, inserting Eq. (63) into Eq. (62), we find

$$\tau_{\text{EKM}} = \frac{128\sqrt{10}}{15\pi} \frac{(1 - e^2)^2}{\sqrt{e}} \tilde{p}^{7/2} \tilde{d}^{-2} \epsilon^{-3/2} M, \quad (64)$$

where  $\tilde{p} \equiv p/M$  and  $\tilde{d} \equiv d/\mu$ . To ensure that the inner orbit remains circular for a sufficiently long time, we require that  $\tau_{\text{EKM}} > 2\pi \times 10^4/\Omega_g$ , i.e., the inner orbit stays circular for at least  $10^4$  outer orbital periods. This timescale suffice to allow significant dephasing between b-EMRI and EMRI, as shown in Fig. 6. In the following analysis, we will set  $e = 0.1$  as an example.

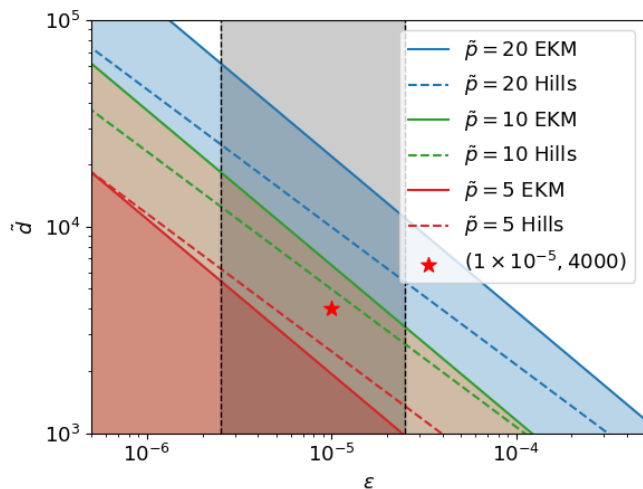


FIG. 7: Parameter space of a b-EMRI. The regions below the solid (dashed) lines satisfy the EKM (stability) condition when  $\tilde{p} = 20, 10, 5$ . The grey shaded region represents a IB in the mass range of  $10M_{\odot} < \mu < 100M_{\odot}$ , where we have assumed  $M = 4 \times 10^6 M_{\odot}$ . The red star denotes our fiducial model in which  $\epsilon = 10^{-5}$ ,  $\tilde{d} = 4000$ .

In Fig. 7 we show the parameter space where the Hill’s condition  $d < R_H/3$  and the EKM condition  $\tau_{\text{EKM}} > 2\pi \times 10^4/\Omega_g$  can be met. We find that for larger  $p$  (e.g.,  $\tilde{p} = 20$ ), the Hill’s condition plays a more important role and sets the upper limit for  $d$ . The EKM condition is more important for smaller  $p$ . The red star in the plot indicates the parameters used in our fiducial model. It lies in a region where both conditions can be met as long as  $p \geq 10M$ .

It is worth noting that even in the case where the IB has some eccentricity, the resonant excitation of QNMs is still valid as long as the inner orbital frequencies match the QNM frequencies. Technically speaking, we can perform a Fourier expansion of the inner orbit, treating the Fourier modes as a series of circular motions. Then our analysis shown above remains applicable to eccentric binaries.

### C. Validity of the model

In Sec. II G we demonstrated how to track the evolution of the system ‘quasi-adiabatically’. In particular, the evolution of the parameter  $p$  is derived assuming oscillating geodesic motion of the OB. In this work, however, we follow Ref. [63, 64] and write the stress-energy tensor

of the IB as

$$T^{\mu\nu}(x) = m_1 \int d\tau \frac{\delta^4(x - z_1(\tau))}{\sqrt{-g(x)}} \frac{dz_1^\mu(\tau)}{d\tau} \frac{dz_1^\nu(\tau)}{d\tau} + m_2 \int d\tau \frac{\delta^4(x - z_2(\tau))}{\sqrt{-g(x)}} \frac{dz_2^\mu(\tau)}{d\tau} \frac{dz_2^\nu(\tau)}{d\tau}, \quad (65)$$

where  $m_1 = m_2 = \mu/2$  and  $z_{1,2}^\mu$  are the trajectories of the two small BHs in the BL coordinates derived as Eq. (10). This  $T^{\mu\nu}$  is missing information about the internal energy and angular momentum of the IB. Because we constructed the background motion of the IB independently of the stress-energy, we cannot guarantee its conservation without adding a term accounting for the interaction of the two monopole particles. For the equal mass IB we consider here, we have  $\nabla_\mu T^{\mu\nu} \propto \mu d^2$ , meaning we are missing some terms at the same order which we keep in the waveform amplitudes and inspiral evolution. In Appendix D, we show how to construct the correction to the stress-energy due to the interaction between the two monopole particles. When this interaction term is included, the stress-energy is conserved through to the order at which we truncate our waveform model and in that sense the model is fully relativistic to that order.

While we have not yet included this interaction term in the stress-energy when solving the Teukolsky equation, we remark that it is straight forward to add in follow up work as a linear correction to the Teukolsky amplitudes (and therefore fluxes). Without accounting for that term, the waveform model should not be used in parameter estimation studies for example. However, its neglect does not change the qualitative features of our findings.

## VI. CONCLUSION AND FUTURE WORK

In this work we have modeled the trajectories of the two stellar-mass BHs in a b-EMRI system using a relativistic coordinate transformation. In turn, we derived the source term in the Teukolsky equation, allowing us to compute the waveform of a b-EMRI using black hole perturbation theory. We find that the transformation of the orbits from the *FFF* into *BL* coordinates introduces both low- and high-frequency perturbations in the source term of the Teukolsky equation. It induces six additional modes proportional to the IB’s separation,  $d$ , and fifteen additional modes proportional to  $d^2$  in the waveform. Our assumption of equal-mass IBs results in the cancellation of the linear  $d$  waveform contributions. Nevertheless, more generic choices of mass for the two small BHs does not introduce significant difficulties in the application of our method.

Our results confirm that the high-frequency perturbation resonantly excites the QNMs of the central SMBH, which was first discovered in Ref. [63]. We further analyzed the condition for the mode excitation and attributed the finite amplitudes of the QNMs to a mismatch

between the real perturbation frequencies and the complex QNM frequencies. The most important finding in this work is that when the QNMs are excited, b-EMRIs evolve faster than standard EMRIs with the same outer parameters ( $M, a, p, \epsilon$ ), because the excited QNMs enhance the energy and angular-momentum fluxes.

Two potential extensions of this work can be carried out in the future. First, the model could be extended to account for the interaction stress-energy of the IB and to a wider range of astrophysical scenarios. For example, one can incorporate eccentricity in the outer binary orbit, as is expected by the formation model of b-EMRIs [39, 40], or evolve the inner orbit dynamically, as has been modeled in Ref. [75]. Second, one can study the distinguishability of b-EMRI systems from normal EMRIs. While this has been examined in Ref. [65] and Ref. [73], our model has revealed new signatures of b-EMRIs, particularly related to  $p$ , such that the b-EMRI system evolves faster during the early inspiral phase before converging to the standard EMRI evolution.

### ACKNOWLEDGMENTS

This work is supported by the National Key Research and Development Program of China (Grant No. 2021YFC2203002) and the National Natural Science Foundation of China (Grant No. 11991053). Y.Y. acknowledges NUS Physics Department for providing comfortable office environment and warm care. Y.Y. would like to thank Haolan Zheng and Han Yan for several inspirational discussions. The authors thank Soichiro Isoyama, Wenbiao Han, and Xilong Fan for insightful feedback on a draft of this paper. J.M. acknowledges support by the NUS Faculty of Science, under the research grant 22-5478-A0001.

### Appendix A: Transformation from the LIF to BL coordinates

The transformation equations between different coordinates have been derived in Ref. [80]. A more general set of transformation equations from Fermi coordinates to other coordinate systems can be found in Ref. [81]. In this work, we use the results from Ref. [80] for co-moving observers on circular orbits. For any circular orbit, the coordinates measured by such an observer are  $(T, X^1, X^2, X^3)$ , where  $T$  is the proper time along the observer's worldline, and  $X^1, X^2, X^3$  represent the three spatial coordinates in the vicinity of the observer. The spatial coordinates  $X^1, X^2, X^3$  are assumed to be small compared to the local curvature radius. The transformation equations between  $(T, X^1, X^2, X^3)$  and the BL coordinates  $(t, r, \theta, \varphi)$  are

$$DT = T - \Omega(\nu)X^1X^3 + \mathcal{O}(3), \quad (\text{A1a})$$

$$\begin{aligned} DR &= X^1 \left( 1 + \frac{1}{2} {}^{(0)}\kappa(r, m)^{\hat{r}} X^1 \right) \\ &\quad - \frac{1}{2} {}^{(0)}\kappa(\theta, m)^{\hat{r}} (X^2)^2 \\ &\quad - \frac{1}{2} {}^{(0)}\kappa(\varphi, U)^{\hat{r}} (X^3)^2 + \mathcal{O}(3), \end{aligned} \quad (\text{A1b})$$

$$D\Theta = X^2 \left( 1 + {}^{(0)}\kappa(\theta, m)^{\hat{r}} X^1 \right) + \mathcal{O}(3), \quad (\text{A1c})$$

$$D\Phi = X^3 \left( 1 + {}^{(0)}\kappa(\varphi, U)^{\hat{r}} X^1 \right) + \mathcal{O}(3), \quad (\text{A1d})$$

where

$$\begin{aligned} DT &= \gamma \left[ {}^{(0)}M(t - t_0) \right. \\ &\quad \left. - \left( {}^{(0)}M^{(0)}M_\varphi + \nu^{(0)}\gamma_{\varphi\varphi}^{1/2} \right) (\varphi - \varphi_0) \right], \end{aligned} \quad (\text{A2a})$$

$$DR = {}^{(0)}\gamma_{rr}^{1/2} (r - r_0), \quad (\text{A2b})$$

$$D\Theta = {}^{(0)}\gamma_{\theta\theta}^{1/2} (\theta - \theta_0), \quad (\text{A2c})$$

$$\begin{aligned} D\Phi &= \gamma \left[ - {}^{(0)}M\nu(t - t_0) \right. \\ &\quad \left. + \left( {}^{(0)}M^{(0)}M_\varphi\nu + {}^{(0)}\gamma_{\varphi\varphi}^{1/2} \right) (\varphi - \varphi_0) \right]. \end{aligned} \quad (\text{A2d})$$

If the circular orbit is geodesic, some of the coefficients are in simpler forms, we denote them as

$$\begin{aligned} \kappa_r &\equiv {}^{(0)}\kappa(r, m)^{\hat{r}}, & \kappa_\theta &\equiv {}^{(0)}\kappa(\theta, m)^{\hat{r}}, \\ \kappa_\varphi &\equiv {}^{(0)}\kappa(\varphi, U)^{\hat{r}}, & \mathcal{M} &\equiv {}^{(0)}M, & \mathcal{M}_\varphi &\equiv {}^{(0)}M_\varphi, \\ \gamma_{rr}^{1/2} &\equiv {}^{(0)}\gamma_{rr}^{1/2}, & \gamma_{\theta\theta}^{1/2} &\equiv {}^{(0)}\gamma_{\theta\theta}^{1/2}, & \gamma_{\varphi\varphi}^{1/2} &\equiv {}^{(0)}\gamma_{\varphi\varphi}^{1/2}. \end{aligned} \quad (\text{A3})$$

Sort  $t, r, \theta, \varphi$  out and write them on the left hand side of the equations, we obtain

$$\begin{aligned} t &= t_0 + \frac{\gamma_{\varphi\varphi}^{1/2} + \mathcal{M}\mathcal{M}_\varphi\nu}{\gamma_{\varphi\varphi}^{1/2}\mathcal{M}/\gamma} T + \frac{\mathcal{M}\mathcal{M}_\varphi + \gamma_{\varphi\varphi}^{1/2}\nu}{\gamma_{\varphi\varphi}^{1/2}\mathcal{M}/\gamma} X^3 \\ &\quad + \frac{(\mathcal{M}\mathcal{M}_\varphi + \gamma_{\varphi\varphi}^{1/2}\nu)\kappa_\varphi - (\gamma_{\varphi\varphi}^{1/2} + \mathcal{M}\mathcal{M}_\varphi\nu)\Omega}{\gamma_{\varphi\varphi}^{1/2}\mathcal{M}/\gamma} X^1 X^3, \end{aligned} \quad (\text{A4a})$$

$$\begin{aligned} r &= r_0 + \frac{1}{\gamma_{rr}^{1/2}} X^1 + \frac{\kappa_r}{2\gamma_{rr}^{1/2}} (X^1)^2 \\ &\quad - \frac{\kappa_\theta}{2\gamma_{rr}^{1/2}} (X^2)^2 - \frac{\kappa_\varphi}{2\gamma_{rr}^{1/2}} (X^3)^2, \end{aligned} \quad (\text{A4b})$$

$$\theta = \theta_0 + \frac{1}{\gamma_{\theta\theta}^{1/2}} X^2 + \frac{\kappa_\theta}{\gamma_{\theta\theta}^{1/2}} X^1 X^2, \quad (\text{A4c})$$

$$\varphi = \varphi_0 + \frac{\nu\gamma}{\gamma_{\varphi\varphi}^{1/2}} T + \frac{\gamma}{\gamma_{\varphi\varphi}^{1/2}} X^3 + \frac{\kappa_\varphi - \nu\Omega}{\gamma_{\varphi\varphi}^{1/2}/\gamma} X^1 X^3. \quad (\text{A4d})$$

where

$$\begin{aligned}
\mathcal{M} &= \sqrt{1 - \frac{2M}{p}}, \quad \mathcal{M}_\varphi = -\frac{2aM}{p-2M}, \\
\Delta_0 &= p^2 - 2Mp + a^2, \quad \Omega = -\sqrt{\frac{M}{p^3}} \\
\gamma_{rr}^{1/2} &= \frac{p}{\sqrt{\Delta_0}}, \quad \gamma_{\theta\theta}^{1/2} = \sqrt{\Delta_0}, \quad \gamma_{\varphi\varphi}^{1/2} = \sqrt{\frac{p\Delta_0}{p-2M}}, \\
\kappa_r &= \frac{Mp - a^2}{p^2\sqrt{\Delta_0}}, \quad \kappa_\theta = -\frac{\sqrt{\Delta_0}}{p^2}, \\
\kappa_\varphi &= \frac{a^2Mp - 4M^2p^2 + 4Mp^3 - p^4 - M\Delta_0}{p^2(p-2M)\sqrt{\Delta_0}}, \\
\nu &= \frac{\sqrt{\Delta_0}}{a + (p-2M)\sqrt{p/M}}, \quad \gamma = \frac{1}{\sqrt{1-\nu^2}}.
\end{aligned} \tag{A5}$$

In our case, we have

$$t_0 = 0, \quad r_0 = p, \quad \theta_0 = \frac{\pi}{2}, \quad \varphi_0 = 0. \tag{A6}$$

It is straightforward to verify that the coefficients of  $T$  in the  $t$  and  $\varphi$  components of Eq. (A4) correspond to the 4-velocity components  $u^t$  and  $u^\varphi$ .

Inserting Eqs. (7)-(8) into Eq. (A4), we obtain the coefficients for the first- and the second-order expansions

$$\begin{aligned}
c_{01} &= \frac{\mathcal{M}\mathcal{M}_\varphi + \gamma_{\varphi\varphi}^{1/2}\nu}{4\gamma_{\varphi\varphi}^{1/2}\mathcal{M}/\gamma} \left\{ (1 - \sin\tilde{\theta}) \sin \left[ (\Omega + \omega_{IB})\tau + \tilde{\psi} \right] \right. \\
&\quad \left. + (1 + \sin\tilde{\theta}) \sin \left[ (\Omega - \omega_{IB})\tau + \tilde{\psi} \right] \right\}, \tag{A7a}
\end{aligned}$$

$$\begin{aligned}
c_{11} &= \frac{1}{4\gamma_{rr}^{1/2}} \left\{ (1 - \sin\tilde{\theta}) \cos \left[ (\Omega + \omega_{IB})\tau + \tilde{\psi} \right] \right. \\
&\quad \left. + (1 + \sin\tilde{\theta}) \cos \left[ (\Omega - \omega_{IB})\tau + \tilde{\psi} \right] \right\}, \tag{A7b}
\end{aligned}$$

$$c_{21} = \frac{1}{2\gamma_{\theta\theta}^{1/2}} \cos\tilde{\theta} \sin(\omega_{IB}\tau), \tag{A7c}$$

$$\begin{aligned}
c_{31} &= \frac{\gamma}{4\gamma_{\varphi\varphi}^{1/2}} \left\{ (1 - \sin\tilde{\theta}) \sin \left[ (\Omega + \omega_{IB})\tau + \tilde{\psi} \right] \right. \\
&\quad \left. + (1 + \sin\tilde{\theta}) \sin \left[ (\Omega - \omega_{IB})\tau + \tilde{\psi} \right] \right\}, \tag{A7d}
\end{aligned}$$

$$\begin{aligned}
c_{02} &= \frac{(\mathcal{M}\mathcal{M}_\varphi + \gamma_{\varphi\varphi}^{1/2}\nu)\kappa_\varphi - (\gamma_{\varphi\varphi}^{1/2} + \mathcal{M}\mathcal{M}_\varphi\nu)\Omega}{32\gamma_{\varphi\varphi}^{1/2}\mathcal{M}/\gamma} \\
&\quad \times \left\{ \left(1 - \sin\tilde{\theta}\right)^2 \sin \left[ 2(\Omega + \omega_{IB})\tau + 2\tilde{\psi} \right] \right. \\
&\quad \left. + \cos^2\tilde{\theta} \sin \left( 2\Omega\tau + 2\tilde{\psi} \right) \right. \\
&\quad \left. + \left(1 + \sin\tilde{\theta}\right)^2 \sin \left[ 2(\Omega - \omega_{IB})\tau + 2\tilde{\psi} \right] \right\}, \tag{A7e}
\end{aligned}$$

$$\begin{aligned}
c_{12} &= \frac{\kappa_r + \kappa_\varphi}{64\gamma_{rr}^{1/2}} \left(1 - \sin\tilde{\theta}\right)^2 \cos \left[ 2(\Omega + \omega_{IB})\tau + 2\tilde{\psi} \right] \\
&\quad + \frac{\kappa_r + \kappa_\varphi}{64\gamma_{rr}^{1/2}} \left(1 + \sin\tilde{\theta}\right)^2 \cos \left[ 2(\Omega - \omega_{IB})\tau + 2\tilde{\psi} \right]
\end{aligned}$$

$$\begin{aligned}
&+ \frac{\kappa_r + \kappa_\varphi}{64\gamma_{rr}^{1/2}} \cos^2\tilde{\theta} \cos \left( 2\Omega\tau + 2\tilde{\psi} \right) \\
&+ \frac{\kappa_r + 4\kappa_\theta - \kappa_\varphi}{64\gamma_{rr}^{1/2}} \cos^2\tilde{\theta} \cos \left( 2\omega_{IB}\tau \right) \\
&+ \frac{\kappa_r - \kappa_\varphi}{32\gamma_{rr}^{1/2}} \left(1 + \sin^2\tilde{\theta}\right) - \frac{\kappa_\theta}{16\gamma_{rr}^{1/2}} \cos^2\tilde{\theta}, \tag{A7f}
\end{aligned}$$

$$\begin{aligned}
c_{22} &= \frac{\kappa_\theta \cos\tilde{\theta}}{16\gamma_{\theta\theta}^{1/2}} \left\{ \left(1 - \sin\tilde{\theta}\right) \sin \left[ (\Omega + 2\omega_{IB})\tau + \tilde{\psi} \right] \right. \\
&\quad \left. - \left(1 + \sin\tilde{\theta}\right) \sin \left[ (\Omega - 2\omega_{IB})\tau + \tilde{\psi} \right] \right. \\
&\quad \left. + 2 \sin\tilde{\theta} \sin \left( \Omega\tau + \tilde{\psi} \right) \right\}, \tag{A7g}
\end{aligned}$$

$$\begin{aligned}
c_{32} &= \frac{\kappa_\varphi - \nu\Omega}{32\gamma_{\varphi\varphi}^{1/2}/\gamma} \times \left\{ \left(1 - \sin\tilde{\theta}\right)^2 \sin \left[ 2(\Omega + \omega_{IB})\tau + 2\tilde{\psi} \right] \right. \\
&\quad \left. + \cos^2\tilde{\theta} \sin \left( 2\Omega\tau + 2\tilde{\psi} \right) \right. \\
&\quad \left. + \left(1 + \sin\tilde{\theta}\right)^2 \sin \left[ 2(\Omega - \omega_{IB})\tau + 2\tilde{\psi} \right] \right\}. \tag{A7h}
\end{aligned}$$

As we can see, these coefficients are all function of  $\tau$ .

## Appendix B: Teukolsky source term

The source term in Eq. (12) is given by  $\hat{T} = 2\rho^{-4}T_4$ , where  $T_4$  a combination of the projected stress-energy tensor defined by

$$\begin{aligned}
T_4 &= \frac{1}{2}\rho^8\bar{\rho}\hat{L}_{-1}[\rho^{-4}\hat{L}_0(\rho^{-2}\bar{\rho}^{-1}T_{nn})] \\
&\quad + \frac{1}{2\sqrt{2}}\rho^8\bar{\rho}\Delta^2\hat{L}_{-1}[\rho^{-4}\bar{\rho}^2\hat{J}_+(\rho^{-2}\bar{\rho}^{-2}\Delta^{-1}T_{\bar{m}n})] \\
&\quad + \frac{1}{4}\rho^8\bar{\rho}\Delta^2\hat{J}_+[\rho^{-4}\hat{J}_+(\rho^{-2}\bar{\rho}T_{\bar{m}m})] \\
&\quad + \frac{1}{2\sqrt{2}}\rho^8\bar{\rho}\Delta^2\hat{J}_+[\rho^{-4}\bar{\rho}^2\Delta^{-1}\hat{L}_{-1}(\rho^{-2}\bar{\rho}^{-2}T_{\bar{m}n})], \tag{B1}
\end{aligned}$$

where the differential operators  $\hat{L}_s$  and  $\hat{J}_+$  are defined as

$$\hat{L}_s = \partial_\theta - \frac{i}{\sin\theta}\partial_\varphi - ia\sin\theta\partial_t + s\cot\theta, \tag{B2a}$$

$$\hat{J}_+ = \partial_r - \frac{1}{\Delta}((r^2 + a^2)\partial_t + a\partial_\varphi). \tag{B2b}$$

Under the NP tetrad

$$l^\mu = \frac{1}{\Delta}(a^2 + r^2, \Delta, 0, a), \tag{B3a}$$

$$n^\mu = \frac{1}{2\Sigma}(a^2 + r^2, -\Delta, 0, a), \tag{B3b}$$

$$m^\mu = \frac{1}{\sqrt{2}(r + ia\cos\theta)} \left( ia\sin\theta, 0, 1, \frac{i}{\sin\theta} \right), \tag{B3c}$$

$$\bar{m}^\mu = \frac{1}{\sqrt{2}(r - ia\cos\theta)} \left( -ia\sin\theta, 0, 1, -\frac{i}{\sin\theta} \right), \tag{B3d}$$

the projected components of the stress-energy tensor read

$$T_{nn} = \mu \frac{C_{nn}}{\sin \theta} \delta [r - r(t)] \delta [\theta - \theta(t)] \delta [\varphi - \varphi(t)], \quad (\text{B4a})$$

$$T_{\bar{m}n} = \mu \frac{C_{\bar{m}n}}{\sin \theta} \delta [r - r(t)] \delta [\theta - \theta(t)] \delta [\varphi - \varphi(t)], \quad (\text{B4b})$$

$$T_{\bar{m}\bar{m}} = \mu \frac{C_{\bar{m}\bar{m}}}{\sin \theta} \delta [r - r(t)] \delta [\theta - \theta(t)] \delta [\varphi - \varphi(t)], \quad (\text{B4c})$$

where

$$C_{nn} = \frac{1}{4\Sigma^3 u^t} \left[ \mathcal{E}(r^2 + a^2) - a\mathcal{L}_z + \Sigma \frac{dr}{d\tau} \right]^2, \quad (\text{B5a})$$

$$C_{\bar{m}n} = -\frac{\rho}{2\sqrt{2}\Sigma u^t} \left[ \mathcal{E}(r^2 + a^2) - a\mathcal{L}_z + \Sigma \frac{dr}{d\tau} \right] \times \left[ i \sin \theta \left( a\mathcal{E} - \frac{\mathcal{L}_z}{\sin^2 \theta} \right) + \Sigma \frac{d\theta}{d\tau} \right], \quad (\text{B5b})$$

$$C_{\bar{m}\bar{m}} = \frac{\rho^2}{2\Sigma u^t} \left[ i \sin \theta \left( a\mathcal{E} - \frac{\mathcal{L}_z}{\sin^2 \theta} \right) + \Sigma \frac{d\theta}{d\tau} \right]^2. \quad (\text{B5c})$$

Start from Eqs. (20) and (22), doing integration by part, we obtain

$$\begin{aligned} Z_{lm}^{\text{in}}(\omega) &= \frac{1}{\mathcal{W}_{lm}(\omega)} \int_{r_+}^{\infty} dr' \frac{R_{lm}^{\text{in}}(r', \omega)}{\Delta'^2} \mathcal{T}_{lm}(r', \omega), \\ &= \frac{\mu}{\mathcal{W}_{lm}(\omega)} \int_{-\infty}^{\infty} dt e^{i\omega t - im\varphi(t)} \\ &\quad \times \left\{ R_{lm}^{\text{in}}(r, \omega) [A_{nn0}(r, \theta(t)) \right. \\ &\quad \quad \quad \left. + A_{\bar{m}n0}(r, \theta(t)) + A_{\bar{m}\bar{m}0}(r, \theta(t))] \right. \\ &\quad \left. - \frac{dR_{lm}^{\text{in}}(r, \omega)}{dr} [A_{\bar{m}n1}(r, \theta(t)) + A_{\bar{m}\bar{m}1}(r, \theta(t))] \right. \\ &\quad \left. + \frac{d^2 R_{lm}^{\text{in}}(r, \omega)}{dr^2} A_{\bar{m}\bar{m}2}(r, \theta(t)) \right\}_{r=r(t)}, \end{aligned} \quad (\text{B6})$$

where

$$A_{nn0}(r, \theta(t)) = \frac{2\sqrt{2}\pi}{\Delta^2} \rho^{-2} \bar{\rho}^{-1} C_{nn} L_1^\dagger \left[ \rho^{-4} L_2^\dagger (\rho^3 S) \right], \quad (\text{B7a})$$

$$\begin{aligned} A_{\bar{m}n0}(r, \theta(t)) &= -\frac{4\sqrt{\pi}}{\Delta} \rho^{-3} C_{\bar{m}n} \\ &\quad \times \left[ \left( L_2^\dagger S \right) \left( \frac{iK}{\Delta} + \rho + \bar{\rho} \right) \right. \\ &\quad \left. - a \sin \theta S \frac{K}{\Delta} (\bar{\rho} - \rho) \right], \end{aligned} \quad (\text{B7b})$$

$$\begin{aligned} A_{\bar{m}\bar{m}0}(r, \theta(t)) &= \sqrt{2\pi} \rho^{-3} \bar{\rho} C_{\bar{m}\bar{m}} S \\ &\quad \times \left[ -i \left( \frac{K}{\Delta} \right)_{,r} - \frac{K^2}{\Delta^2} + 2i\rho \frac{K}{\Delta} \right], \end{aligned} \quad (\text{B7c})$$

$$\begin{aligned} A_{\bar{m}n1}(r, \theta(t)) &= -\frac{4\sqrt{\pi}}{\Delta} \rho^{-3} C_{\bar{m}n} \\ &\quad \times \left[ L_2^\dagger S + ia \sin \theta (\bar{\rho} - \rho) S \right], \end{aligned} \quad (\text{B7d})$$

$$A_{\bar{m}\bar{m}1}(r, \theta(t)) = 2\sqrt{2\pi} \rho^{-3} \bar{\rho} C_{\bar{m}\bar{m}} S \left( i \frac{K}{\Delta} + \rho \right), \quad (\text{B7e})$$

$$A_{\bar{m}\bar{m}2}(r, \theta(t)) = \sqrt{2\pi} \rho^{-3} \bar{\rho} C_{\bar{m}\bar{m}} S. \quad (\text{B7f})$$

Here the operator in Eq. (B2) takes a new form due to variable separation

$$L_s^\dagger = \partial_\theta + \frac{m}{\sin \theta} - a\omega \sin \theta + s \cot \theta, \quad (\text{B8a})$$

$$J_+ = \partial_r + iK/\Delta. \quad (\text{B8b})$$

Then by replacing the variable of integration from  $t$  to  $\tau$ , we obtain Eq. (26). Note that  $dt/d\tau$  cancels the  $u^t$  in the denominator of Eq. (B5).

### Appendix C: Analytical expressions of split amplitudes

Inserting Eqs. (28) and (30) into Eq. (32), we derive the expression of  $Z_{lm}^{(1)}$  and  $Z_{lm}^{(2)}$ . The first order amplitudes take the form of

$$\begin{aligned} Z_{lm}^{(1)}(\tau, \omega) &= [\alpha_1 c_{01} + \alpha_2 c_{11} + \alpha_3 c_{21} \\ &\quad + \alpha_4 c_{31} + \alpha_5 \partial_\tau c_{11} + \alpha_6 \partial_\tau c_{21}] \\ &\quad \times \exp [i(\omega u^t - mu^\varphi) \tau], \end{aligned} \quad (\text{C1})$$

where  $\alpha_1, \alpha_2, \alpha_3, \alpha_4, \alpha_5, \alpha_6$  are some constants when we fix  $r_0 = p$  and  $\theta_0 = \pi/2$ . Terms like  $\partial_\tau c_{11}$  and  $\partial_\tau c_{21}$  appear because there are  $dr/d\tau, d\theta/d\tau$  in  $C_{nn}, C_{\bar{m}n}, C_{\bar{m}\bar{m}}$  as defined in Eq. (B5). By matching the analytical expressions of  $c_{01}, c_{11}, c_{21}, c_{31}, \partial_\tau c_{11}, \partial_\tau c_{21}$  using *Mathematica*, it's not hard to obtain their expressions. However, due to their length, we will not show them here. Finally, by applying Eq. (A7), we can further expand our results as combinations of sin and cos terms,

$$\begin{aligned} Z_{lm}^{(1)}(\tau, \omega) &= \{ \tilde{\alpha}_1 \sin [(\Omega + \omega_{IB}) \tau + \tilde{\psi}] \\ &\quad + \tilde{\alpha}_2 \cos [(\Omega + \omega_{IB}) \tau + \tilde{\psi}] \\ &\quad + \tilde{\alpha}_3 \sin [(\Omega - \omega_{IB}) \tau + \tilde{\psi}] \\ &\quad + \tilde{\alpha}_4 \cos [(\Omega - \omega_{IB}) \tau + \tilde{\psi}] \\ &\quad + \tilde{\alpha}_5 \sin (\omega_{IB} \tau) + \tilde{\alpha}_6 \cos (\omega_{IB} \tau) \} \\ &\quad \times \exp [i(\omega u^t - mu^\varphi) \tau]. \end{aligned} \quad (\text{C2})$$

Then using Eq. (35) we obtain

$$\begin{aligned} Z_{lm}^{(1)}(\tau, \omega) &= Z_{lm-1-1}^{(1)} \exp [i(\omega u^t - mu^\varphi + \Omega + \omega_{IB}) \tau] \\ &\quad + Z_{lm11}^{(1)} \exp [i(\omega u^t - mu^\varphi - \Omega - \omega_{IB}) \tau] \\ &\quad + Z_{lm-11}^{(1)} \exp [i(\omega u^t - mu^\varphi + \Omega - \omega_{IB}) \tau] \\ &\quad + Z_{lm1-1}^{(1)} \exp [i(\omega u^t - mu^\varphi - \Omega + \omega_{IB}) \tau] \\ &\quad + Z_{lm0-1}^{(1)} \exp [i(\omega u^t - mu^\varphi + \omega_{IB}) \tau] \\ &\quad + Z_{lm01}^{(1)} \exp [i(\omega u^t - mu^\varphi - \omega_{IB}) \tau]. \end{aligned} \quad (\text{C3})$$



This leads to the frequency spectrum when we do the integration in Eq. (31). Meanwhile, the coefficients of the exponential terms are the split amplitudes

$$Z_{lm-1-1}^{(1)} = \frac{-i\tilde{\alpha}_1 + \tilde{\alpha}_2}{2} e^{i\tilde{\psi}}, \quad (\text{C4a})$$

$$Z_{lm-11}^{(1)} = \frac{-i\tilde{\alpha}_3 + \tilde{\alpha}_4}{2} e^{i\tilde{\psi}}, \quad (\text{C4b})$$

$$Z_{lm0-1}^{(1)} = \frac{-i\tilde{\alpha}_5 + \tilde{\alpha}_6}{2}, \quad (\text{C4c})$$

$$Z_{lm01}^{(1)} = \frac{i\tilde{\alpha}_5 + \tilde{\alpha}_6}{2}, \quad (\text{C4d})$$

$$Z_{lm1-1}^{(1)} = \frac{i\tilde{\alpha}_3 + \tilde{\alpha}_4}{2} e^{-i\tilde{\psi}}, \quad (\text{C4e})$$

$$Z_{lm11}^{(1)} = \frac{i\tilde{\alpha}_1 + \tilde{\alpha}_2}{2} e^{-i\tilde{\psi}}, \quad (\text{C4f})$$

where

$$\tilde{\alpha}_1 = \frac{\gamma(1 - \sin\tilde{\theta})}{4\gamma_{\varphi\varphi}^{1/2}} \left[ \alpha_1 \frac{\mathcal{M}\mathcal{M}_\varphi + \gamma_{\varphi\varphi}^{1/2}\nu}{\mathcal{M}} + \alpha_4 \right]$$

$$- \frac{(\Omega + \omega_{IB})(1 - \sin\tilde{\theta})}{4\gamma_{rr}^{1/2}} \alpha_5, \quad (\text{C5a})$$

$$\tilde{\alpha}_2 = \frac{1 - \sin\tilde{\theta}}{4\gamma_{rr}^{1/2}} \alpha_2, \quad (\text{C5b})$$

$$\tilde{\alpha}_3 = \frac{\gamma(1 + \sin\tilde{\theta})}{4\gamma_{\varphi\varphi}^{1/2}} \left[ \alpha_1 \frac{\mathcal{M}\mathcal{M}_\varphi + \gamma_{\varphi\varphi}^{1/2}\nu}{\mathcal{M}} + \alpha_4 \right] - \frac{(\Omega - \omega_{IB})(1 + \sin\tilde{\theta})}{4\gamma_{rr}^{1/2}} \alpha_5, \quad (\text{C5c})$$

$$\tilde{\alpha}_4 = \frac{1 + \sin\tilde{\theta}}{4\gamma_{rr}^{1/2}} \alpha_2, \quad (\text{C5d})$$

$$\tilde{\alpha}_5 = \frac{\cos\tilde{\theta}}{2\gamma_{\theta\theta}^{1/2}} \alpha_3, \quad (\text{C5e})$$

$$\tilde{\alpha}_6 = \frac{\omega_{IB} \cos\tilde{\theta}}{2\gamma_{\theta\theta}^{1/2}} \alpha_6. \quad (\text{C5f})$$

For second order amplitudes, we use the same method. Analogous to Eq. (C1), we have

$$\begin{aligned} Z_{lm}^{(2)}(\tau, \omega) = & \{ \beta_{00}c_{01}c_{01} + \beta_{01}c_{11}c_{11} + \beta_{02}c_{21}c_{21} + \beta_{03}c_{31}c_{31} + \beta_{04}c_{01}c_{11} + \beta_{05}c_{01}c_{21} + \beta_{06}c_{01}c_{31} \\ & + \beta_{07}c_{11}c_{21} + \beta_{08}c_{11}c_{31} + \beta_{09}c_{21}c_{31} + \beta_{0a}c_{02} + \beta_{0b}c_{12} + \beta_{0c}c_{22} + \beta_{0d}c_{32} \\ & + \beta_{10}c_{01}c'_{11} + \beta_{11}c_{01}c'_{21} + \beta_{12}c_{11}c'_{11} + \beta_{13}c_{11}c'_{21} + \beta_{14}c_{21}c'_{11} + \beta_{15}c_{21}c'_{21} + \beta_{16}c_{31}c'_{11} + \beta_{17}c_{31}c'_{21} \\ & + \beta_{20}c'_{11}c'_{11} + \beta_{21}c'_{21}c'_{21} + \beta_{22}c'_{11}c'_{21} + \beta_{23}c'_{12} + \beta_{24}c'_{22} \} \exp [i(\omega u^t - m u^\varphi) \tau]. \end{aligned} \quad (\text{C6})$$

Here prime denotes derivative with respect to  $\tau$ . By matching coefficients, we obtain the analytical expressions of these  $\beta$ . Now we need to incorporate the sin and cos terms into the exponential terms to gain the frequency spectrum. To shorten the expressions, we will update the notations used in Eq. (A7), as the original one are too lengthy to present in full. We rewrite them as

$$c_{01} = \vartheta_{11} \sin [(\Omega + \omega_{IB})\tau + \tilde{\psi}] + \vartheta_{12} \sin [(\Omega - \omega_{IB})\tau + \tilde{\psi}], \quad (\text{C7a})$$

$$c_{11} = \vartheta_{21} \cos [(\Omega + \omega_{IB})\tau + \tilde{\psi}] + \vartheta_{22} \cos [(\Omega - \omega_{IB})\tau + \tilde{\psi}], \quad (\text{C7b})$$

$$c'_{11} = \vartheta'_{21} \sin [(\Omega + \omega_{IB})\tau + \tilde{\psi}] + \vartheta'_{22} \sin [(\Omega - \omega_{IB})\tau + \tilde{\psi}], \quad (\text{C7c})$$

$$c_{21} = \vartheta_{31} \sin(\omega_{IB}\tau), \quad (\text{C7d})$$

$$c'_{21} = \vartheta'_{31} \cos(\omega_{IB}\tau), \quad (\text{C7e})$$

$$c_{31} = \vartheta_{41} \sin [(\Omega + \omega_{IB})\tau + \tilde{\psi}]$$

$$+ \vartheta_{42} \sin [(\Omega - \omega_{IB})\tau + \tilde{\psi}], \quad (\text{C7f})$$

$$\begin{aligned} c_{02} = & \vartheta_{51} \sin [2(\Omega + \omega_{IB})\tau + 2\tilde{\psi}] \\ & + \vartheta_{52} \sin (2\Omega\tau + 2\tilde{\psi}) \\ & + \vartheta_{53} \sin [2(\Omega - \omega_{IB})\tau + 2\tilde{\psi}], \end{aligned} \quad (\text{C7g})$$

$$\begin{aligned} c_{12} = & \vartheta_{61} \cos [2(\Omega + \omega_{IB})\tau + 2\tilde{\psi}] \\ & + \vartheta_{62} \cos (2\Omega\tau + 2\tilde{\psi}) \\ & + \vartheta_{63} \cos [2(\Omega - \omega_{IB})\tau + 2\tilde{\psi}] \\ & + \vartheta_{64} \cos(2\omega_{IB}\tau) + \vartheta_{65}, \end{aligned} \quad (\text{C7h})$$

$$\begin{aligned} c'_{12} = & \vartheta'_{61} \sin [2(\Omega + \omega_{IB})\tau + 2\tilde{\psi}] \\ & + \vartheta'_{62} \sin (2\Omega\tau + 2\tilde{\psi}) \\ & + \vartheta'_{63} \sin [2(\Omega - \omega_{IB})\tau + 2\tilde{\psi}] \\ & + \vartheta'_{64} \sin(2\omega_{IB}\tau), \end{aligned} \quad (\text{C7i})$$

$$\begin{aligned} c_{22} = & \vartheta_{71} \sin [(\Omega + 2\omega_{IB})\tau + \tilde{\psi}] \\ & + \vartheta_{72} \sin [(\Omega - 2\omega_{IB})\tau + \tilde{\psi}] \end{aligned}$$

$$\begin{aligned}
& + \vartheta_{73} \sin(\Omega\tau + \tilde{\psi}), \quad (\text{C7j}) \\
c'_{22} &= \vartheta'_{71} \cos[(\Omega + 2\omega_{IB})\tau + \tilde{\psi}] \\
& + \vartheta'_{72} \cos[(\Omega - 2\omega_{IB})\tau + \tilde{\psi}] \\
& + \vartheta'_{73} \cos(\Omega\tau + \tilde{\psi}), \quad (\text{C7k}) \\
c_{32} &= \vartheta_{81} \sin[2(\Omega + \omega_{IB})\tau + 2\tilde{\psi}] \\
& + \vartheta_{82} \sin(2\Omega\tau + 2\tilde{\psi}) \\
& + \vartheta_{83} \sin[2(\Omega - \omega_{IB})\tau + 2\tilde{\psi}]. \quad (\text{C7l})
\end{aligned}$$

where

$$\vartheta_{11} = \frac{\mathcal{M}\mathcal{M}_\varphi + \gamma_{\varphi\varphi}^{1/2}\nu}{4\gamma_{\varphi\varphi}^{1/2}\mathcal{M}/\gamma} (1 - \sin\tilde{\theta}), \quad (\text{C8a})$$

$$\vartheta_{12} = \frac{\mathcal{M}\mathcal{M}_\varphi + \gamma_{\varphi\varphi}^{1/2}\nu}{4\gamma_{\varphi\varphi}^{1/2}\mathcal{M}/\gamma} (1 + \sin\tilde{\theta}), \quad (\text{C8b})$$

$$\vartheta_{21} = \frac{1}{4\gamma_{rr}^{1/2}} (1 - \sin\tilde{\theta}), \quad (\text{C8c})$$

$$\vartheta_{22} = \frac{1}{4\gamma_{rr}^{1/2}} (1 + \sin\tilde{\theta}), \quad (\text{C8d})$$

$$\vartheta'_{21} = -(\Omega + \omega_{IB})\vartheta_{21}, \quad (\text{C8e})$$

$$\vartheta'_{22} = -(\Omega - \omega_{IB})\vartheta_{22}, \quad (\text{C8f})$$

$$\vartheta_{31} = \frac{1}{2\gamma_{\theta\theta}^{1/2}} \cos\tilde{\theta}, \quad (\text{C8g})$$

$$\vartheta'_{31} = \omega_{IB}\vartheta_{31}, \quad (\text{C8h})$$

$$\vartheta_{41} = \frac{\gamma}{4\gamma_{\varphi\varphi}^{1/2}} (1 - \sin\tilde{\theta}), \quad (\text{C8i})$$

$$\vartheta_{42} = \frac{\gamma}{4\gamma_{\varphi\varphi}^{1/2}} (1 + \sin\tilde{\theta}), \quad (\text{C8j})$$

$$\vartheta_{51} = \Theta_0 (1 - \sin\tilde{\theta})^2, \quad (\text{C8k})$$

$$\vartheta_{52} = \Theta_0 \cos^2\tilde{\theta}, \quad (\text{C8l})$$

$$\vartheta_{53} = \Theta_0 (1 + \sin\tilde{\theta})^2, \quad (\text{C8m})$$

$$\Theta_0 = \frac{(\mathcal{M}\mathcal{M}_\varphi + \gamma_{\varphi\varphi}^{1/2}\nu)\kappa_\varphi - (\gamma_{\varphi\varphi}^{1/2} + \mathcal{M}\mathcal{M}_\varphi\nu)\Omega}{32\gamma_{\varphi\varphi}^{1/2}\mathcal{M}/\gamma}, \quad (\text{C8n})$$

$$\vartheta_{61} = \frac{\kappa_r + \kappa_\varphi}{64\gamma_{rr}^{1/2}} (1 - \sin\tilde{\theta})^2, \quad (\text{C8o})$$

$$\vartheta_{62} = \frac{\kappa_r + \kappa_\varphi}{64\gamma_{rr}^{1/2}} \cos^2\tilde{\theta}, \quad (\text{C8p})$$

$$\vartheta_{63} = \frac{\kappa_r + \kappa_\varphi}{64\gamma_{rr}^{1/2}} (1 + \sin\tilde{\theta})^2, \quad (\text{C8q})$$

$$\vartheta_{64} = \frac{\kappa_r + 4\kappa_\theta - \kappa_\varphi}{64\gamma_{rr}^{1/2}} \cos^2\tilde{\theta}, \quad (\text{C8r})$$

$$\vartheta_{65} = \frac{\kappa_r - \kappa_\varphi}{32\gamma_{rr}^{1/2}} (1 + \sin^2\tilde{\theta}) - \frac{\kappa_\theta}{16\gamma_{rr}^{1/2}} \cos^2\tilde{\theta}, \quad (\text{C8s})$$

$$\vartheta'_{61} = -2(\Omega + \omega_{IB})\vartheta_{61}, \quad (\text{C8t})$$

$$\vartheta'_{62} = -2\Omega\vartheta_{62}, \quad (\text{C8u})$$

$$\vartheta'_{63} = -2(\Omega - \omega_{IB})\vartheta_{63}, \quad (\text{C8v})$$

$$\vartheta'_{64} = -2\omega_{IB}\vartheta_{64}, \quad (\text{C8w})$$

$$\vartheta_{71} = \frac{\kappa_\theta \cos\tilde{\theta}}{16\gamma_{\theta\theta}^{1/2}} (1 - \sin\tilde{\theta}), \quad (\text{C8x})$$

$$\vartheta_{72} = -\frac{\kappa_\theta \cos\tilde{\theta}}{16\gamma_{\theta\theta}^{1/2}} (1 + \sin\tilde{\theta}), \quad (\text{C8y})$$

$$\vartheta_{73} = \frac{\kappa_\theta}{16\gamma_{\theta\theta}^{1/2}} \sin(2\tilde{\theta}), \quad (\text{C8z})$$

$$\vartheta'_{71} = (\Omega + 2\omega_{IB})\vartheta_{71}, \quad (\text{C8aa})$$

$$\vartheta'_{72} = (\Omega - 2\omega_{IB})\vartheta_{72}, \quad (\text{C8bb})$$

$$\vartheta'_{73} = \Omega\vartheta_{73}, \quad (\text{C8cc})$$

$$\vartheta_{81} = \frac{\kappa_\varphi - \nu\Omega}{32\gamma_{\varphi\varphi}^{1/2}/\gamma} (1 - \sin\tilde{\theta})^2, \quad (\text{C8dd})$$

$$\vartheta_{82} = \frac{\kappa_\varphi - \nu\Omega}{32\gamma_{\varphi\varphi}^{1/2}/\gamma} \cos^2\tilde{\theta}, \quad (\text{C8ee})$$

$$\vartheta_{83} = \frac{\kappa_\varphi - \nu\Omega}{32\gamma_{\varphi\varphi}^{1/2}/\gamma} (1 + \sin\tilde{\theta})^2. \quad (\text{C8ff})$$

Analogous to Eq. (C4), the split amplitudes for the second order expansion are given by

$$\begin{aligned}
Z_{lm-2-2}^{(2)} &= -\frac{1}{4} [\beta_{00}\vartheta_{11}^2 - \beta_{01}\vartheta_{21}^2 + \beta_{20}\vartheta_{21}^2 + \beta_{03}\vartheta_{41}^2 + \beta_{10}\vartheta_{11}\vartheta'_{21} + \beta_{06}\vartheta_{11}\vartheta_{41} + \beta_{16}\vartheta'_{21}\vartheta_{41}] \\
&\quad - \frac{1}{4} i [\beta_{04}\vartheta_{11}\vartheta_{21} + \beta_{12}\vartheta_{21}\vartheta'_{21} + \beta_{08}\vartheta_{21}\vartheta_{41}] + \frac{1}{2} (\beta_{0a} + \beta_{0b}) \vartheta_{61} - \frac{1}{2} i (\beta_{21}\vartheta'_{61} + \beta_{0d}\vartheta_{81}), \quad (\text{C9a})
\end{aligned}$$

$$\begin{aligned}
Z_{lm-20}^{(2)} &= -\frac{1}{4} [\beta_{10} (\vartheta_{12}\vartheta'_{21} + \vartheta_{11}\vartheta'_{22}) + \beta_{06} (\vartheta_{12}\vartheta_{41} + \vartheta_{11}\vartheta_{42}) + \beta_{16} (\vartheta'_{22}\vartheta_{41} + \vartheta'_{21}\vartheta_{42})] \\
&\quad - \frac{1}{4} i [\beta_{04} (\vartheta_{12}\vartheta_{21} + \vartheta_{11}\vartheta_{22}) + \beta_{12} (\vartheta'_{21}\vartheta_{22} + \vartheta_{21}\vartheta'_{22}) + \beta_{08} (\vartheta_{22}\vartheta_{41} + \vartheta_{21}\vartheta_{42})] \\
&\quad + \frac{1}{2} [-\beta_{00}\vartheta_{11}\vartheta_{12} + \beta_{01}\vartheta_{21}\vartheta_{22} - \beta_{20}\vartheta'_{21}\vartheta'_{22} - \beta_{03}\vartheta_{41}\vartheta_{42} + (\beta_{0a} + \beta_{0b}) \vartheta_{62}]
\end{aligned}$$

$$-\frac{1}{2}i(\beta_{23}\vartheta'_{62} + \beta_{0d}\vartheta_{82}), \quad (\text{C9b})$$

$$\begin{aligned} Z_{lm-22}^{(2)} = & -\frac{1}{4}[\beta_{00}\vartheta_{12}^2 - \beta_{01}\vartheta_{22}^2 + \beta_{20}\vartheta'_{22} + \beta_{03}\vartheta_{42}^2 + \beta_{10}\vartheta_{12}\vartheta'_{22} + \beta_{06}\vartheta_{12}\vartheta_{42} + \beta_{16}\vartheta'_{22}\vartheta_{42}] \\ & -\frac{1}{4}[\beta_{04}\vartheta_{12}\vartheta_{22} + \beta_{12}\vartheta_{22}\vartheta'_{22} + \beta_{08}\vartheta_{22}\vartheta_{42}] + \frac{1}{2}(\beta_{0a} + \beta_{0b})\vartheta_{63} - \frac{1}{2}i(\beta_{23}\vartheta'_{63} + \beta_{0d}\vartheta_{83}), \end{aligned} \quad (\text{C9c})$$

$$\begin{aligned} Z_{lm-1-2}^{(2)} = & -\frac{1}{4}[\beta_{05}\vartheta_{11}\vartheta_{31} + \beta_{09}\vartheta_{31}\vartheta_{41} + \beta_{14}\vartheta'_{21}\vartheta_{31} - \beta_{13}\vartheta_{21}\vartheta'_{31}] + \frac{1}{2}\beta_{24}\vartheta'_{71} \\ & -\frac{1}{4}i[\beta_{07}\vartheta_{21}\vartheta_{31} + \beta_{11}\vartheta_{11}\vartheta'_{31} + \beta_{17}\vartheta'_{31}\vartheta_{41} + \beta_{22}\vartheta'_{21}\vartheta'_{31}] - \frac{1}{2}i\beta_{0c}\vartheta_{71}, \end{aligned} \quad (\text{C9d})$$

$$\begin{aligned} Z_{lm-10}^{(2)} = & \frac{1}{4}[\beta_{05}\vartheta_{31}(\vartheta_{11} - \vartheta_{12}) + \beta_{14}\vartheta_{31}(\vartheta'_{21} - \vartheta'_{22}) + \beta_{13}\vartheta'_{31}(\vartheta_{21} + \vartheta_{22}) + \beta_{09}\vartheta_{31}(\vartheta_{41} - \vartheta_{42})] \\ & -\frac{1}{4}i[\beta_{07}\vartheta_{31}(\vartheta_{22} - \vartheta_{21}) + \beta_{11}\vartheta'_{31}(\vartheta_{11} + \vartheta_{12}) + \beta_{22}\vartheta'_{31}(\vartheta'_{21} + \vartheta'_{22}) + \beta_{17}\vartheta'_{31}(\vartheta_{41} + \vartheta_{42})] \\ & -\frac{1}{2}i\beta_{0c}\vartheta_{73} + \frac{1}{2}\beta_{24}\vartheta'_{73}, \end{aligned} \quad (\text{C9e})$$

$$\begin{aligned} Z_{lm-12}^{(2)} = & \frac{1}{4}[\beta_{05}\vartheta_{12}\vartheta_{31} + \beta_{14}\vartheta'_{22}\vartheta_{31} + \beta_{13}\vartheta_{22}\vartheta'_{31} + \beta_{09}\vartheta_{31}\vartheta_{42}] + \frac{1}{2}\beta_{24}\vartheta'_{72} \\ & + \frac{1}{4}i[\beta_{11}\vartheta_{12}\vartheta'_{31} - \beta_{07}\vartheta'_{22}\vartheta_{31} + \beta_{22}\vartheta'_{22}\vartheta'_{31} + \beta_{17}\vartheta'_{31}\vartheta_{42}] + \frac{1}{2}i\beta_{0c}\vartheta_{72}, \end{aligned} \quad (\text{C9f})$$

$$\begin{aligned} Z_{lm0-2}^{(2)} = & \frac{1}{2}[\beta_{00}\vartheta_{11}\vartheta_{12} + \beta_{01}\vartheta_{21}\vartheta_{22} + \beta_{20}\vartheta'_{21}\vartheta'_{22} + \beta_{03}\vartheta_{41}\vartheta_{42} + (\beta_{0a} + \beta_{0b})\vartheta_{64}] - \frac{1}{2}i\beta_{23}\vartheta'_{64} \\ & + \frac{1}{4}[\beta_{10}(\vartheta_{12}\vartheta'_{21} + \vartheta_{11}\vartheta'_{22}) + \beta_{21}\vartheta_{31}^2 + \beta_{16}(\vartheta'_{22}\vartheta_{41} + \vartheta'_{21}\vartheta_{42}) + \beta_{06}(\vartheta_{11}\vartheta_{42} + \vartheta_{12}\vartheta_{41}) - \beta_{02}\vartheta_{31}^2] \\ & + \frac{1}{4}i[\beta_{04}(\vartheta_{12}\vartheta_{21} - \vartheta_{11}\vartheta_{22}) + \beta_{12}(\vartheta_{21}\vartheta'_{22} - \vartheta'_{21}\vartheta_{22}) + \beta_{08}(-\vartheta_{22}\vartheta_{41} + \vartheta_{21}\vartheta_{42}) - \beta_{15}\vartheta_{31}\vartheta'_{31}], \end{aligned} \quad (\text{C9g})$$

$$\begin{aligned} Z_{lm00}^{(2)} = & \frac{1}{2}[\beta_{00}(\vartheta_{11}^2 + \vartheta_{12}^2) + \beta_{01}(\vartheta_{21}^2 + \vartheta_{22}^2) + \beta_{10}(\vartheta_{11}\vartheta'_{21} + \vartheta_{12}\vartheta'_{22}) + \beta_{20}(\vartheta_{21}^2 + \vartheta_{22}^2) \\ & + \beta_{02}\vartheta_{31}^2 + \beta_{21}\vartheta_{31}^2 + \beta_{06}(\vartheta_{11}\vartheta_{41} + \vartheta_{12}\vartheta_{42}) + \beta_{16}(\vartheta'_{21}\vartheta_{41} + \vartheta'_{22}\vartheta_{42}) + \beta_{03}(\vartheta_{41}^2 + \vartheta_{42}^2)] \\ & + (\beta_{0a} + \beta_{0b})\vartheta_{65}, \end{aligned} \quad (\text{C9h})$$

$$\begin{aligned} Z_{lm02}^{(2)} = & \frac{1}{2}[\beta_{00}\vartheta_{11}\vartheta_{12} + \beta_{01}\vartheta_{21}\vartheta_{22} + \beta_{20}\vartheta'_{21}\vartheta'_{22} + \beta_{03}\vartheta_{41}\vartheta_{42} + (\beta_{0a} + \beta_{0b})\vartheta_{64}] + \frac{1}{2}i\beta_{23}\vartheta'_{64} \\ & + \frac{1}{4}[\beta_{10}(\vartheta_{12}\vartheta'_{21} + \vartheta_{11}\vartheta'_{22}) + \beta_{21}\vartheta_{31}^2 + \beta_{16}(\vartheta'_{22}\vartheta_{41} + \vartheta'_{21}\vartheta_{42}) + \beta_{06}(\vartheta_{11}\vartheta_{42} + \vartheta_{12}\vartheta_{41}) - \beta_{02}\vartheta_{31}^2] \\ & + \frac{1}{4}i[\beta_{04}(\vartheta_{11}\vartheta_{22} - \vartheta_{12}\vartheta_{21}) + \beta_{12}(\vartheta'_{21}\vartheta_{22} - \vartheta_{21}\vartheta'_{22}) + \beta_{08}(\vartheta_{22}\vartheta_{41} - \vartheta_{21}\vartheta_{42}) + \beta_{15}\vartheta_{31}\vartheta'_{31}], \end{aligned} \quad (\text{C9i})$$

$$\begin{aligned} Z_{lm1-2}^{(2)} = & \frac{1}{4}[\beta_{05}\vartheta_{12}\vartheta_{31} + \beta_{14}\vartheta'_{22}\vartheta_{31} + \beta_{13}\vartheta_{22}\vartheta'_{31} + \beta_{09}\vartheta_{31}\vartheta_{42}] + \frac{1}{2}\beta_{24}\vartheta'_{72} \\ & + \frac{1}{4}i[-\beta_{07}\vartheta_{22}\vartheta_{31} + \beta_{11}\vartheta_{12}\vartheta'_{31} + \beta_{22}\vartheta'_{22}\vartheta'_{31} + \beta_{17}\vartheta'_{31}\vartheta_{42}] + \frac{1}{2}i\beta_{0c}\vartheta_{72}, \end{aligned} \quad (\text{C9j})$$

$$\begin{aligned} Z_{lm10}^{(2)} = & \frac{1}{4}[\beta_{05}\vartheta_{31}(\vartheta_{11} - \vartheta_{12}) + \beta_{14}\vartheta_{31}(\vartheta'_{21} - \vartheta'_{22}) + \beta_{13}\vartheta'_{31}(\vartheta_{21} + \vartheta_{22}) + \beta_{09}\vartheta_{31}(\vartheta_{41} - \vartheta_{42})] \\ & + \frac{1}{4}i[\beta_{07}\vartheta_{31}(\vartheta_{22} - \vartheta_{21}) + \beta_{11}\vartheta'_{31}(\vartheta_{11} + \vartheta_{12}) + \beta_{22}\vartheta'_{31}(\vartheta'_{21} + \vartheta'_{22}) + \beta_{17}\vartheta'_{31}(\vartheta_{41} + \vartheta_{42})] \\ & + \frac{1}{2}i\beta_{0c}\vartheta_{73} + \frac{1}{2}\beta_{24}\vartheta'_{73}, \end{aligned} \quad (\text{C9k})$$

$$\begin{aligned} Z_{lm12}^{(2)} = & -\frac{1}{4}[\beta_{05}\vartheta_{11}\vartheta_{31} + \beta_{14}\vartheta'_{21}\vartheta_{31} - \beta_{13}\vartheta_{21}\vartheta'_{31} + \beta_{09}\vartheta_{31}\vartheta_{41}] + \frac{1}{2}\beta_{24}\vartheta'_{71} \\ & + \frac{1}{4}i[\beta_{07}\vartheta_{21}\vartheta_{31} + \beta_{11}\vartheta_{11}\vartheta'_{31} + \beta_{22}\vartheta'_{21}\vartheta'_{31} + \beta_{17}\vartheta'_{31}\vartheta_{41}] + \frac{1}{2}i\beta_{0c}\vartheta_{71}, \end{aligned} \quad (\text{C9l})$$

$$\begin{aligned} Z_{lm2-2}^{(2)} = & -\frac{1}{4}[\beta_{00}\vartheta_{12}^2 - \beta_{01}\vartheta_{22}^2 + \beta_{20}\vartheta'_{22} + \beta_{03}\vartheta_{42}^2 + \beta_{10}\vartheta_{12}\vartheta'_{22} + \beta_{06}\vartheta_{12}\vartheta_{42} + \beta_{16}\vartheta'_{22}\vartheta_{42}] \\ & + \frac{1}{4}i[\beta_{04}\vartheta_{12}\vartheta_{22} + \beta_{12}\vartheta_{22}\vartheta'_{22} + \beta_{08}\vartheta_{22}\vartheta_{42}] + \frac{1}{2}(\beta_{0a} + \beta_{0b})\vartheta_{63} + \frac{1}{2}i(\beta_{23}\vartheta'_{63} + \beta_{0d}\vartheta_{83}), \end{aligned} \quad (\text{C9m})$$

$$\begin{aligned}
Z_{lm20}^{(2)} = & -\frac{1}{4} [\beta_{10} (\vartheta_{12}\vartheta'_{21} + \vartheta_{11}\vartheta'_{22}) + \beta_{06} (\vartheta_{12}\vartheta_{41} + \vartheta_{11}\vartheta_{42}) + \beta_{16} (\vartheta'_{22}\vartheta_{41} + \vartheta'_{21}\vartheta_{42})] \\
& + \frac{1}{4} i [\beta_{04} (\vartheta_{12}\vartheta_{21} - \vartheta_{11}\vartheta_{22}) + \beta_{12} (\vartheta'_{21}\vartheta_{22} + \vartheta_{21}\vartheta'_{22}) + \beta_{08} (\vartheta_{22}\vartheta_{41} + \vartheta_{21}\vartheta_{42})] \\
& + \frac{1}{2} [-\beta_{00}\vartheta_{11}\vartheta_{12} + \beta_{01}\vartheta_{21}\vartheta_{22} - \beta_{20}\vartheta'_{21}\vartheta'_{22} - \beta_{03}\vartheta_{41}\vartheta_{42} + (\beta_{0a} + \beta_{0b})\vartheta_{62}] + \frac{1}{2} i (\beta_{23}\vartheta'_{62} + \beta_{0d}\vartheta_{82}), \quad (\text{C9n})
\end{aligned}$$

$$\begin{aligned}
Z_{lm22}^{(2)} = & -\frac{1}{4} [\beta_{00}\vartheta_{11}^2 - \beta_{01}\vartheta_{21}^2 + \beta_{20}\vartheta'_{21}^2 + \beta_{03}\vartheta_{41}^2] + \frac{1}{4} i [\beta_{04}\vartheta_{11}\vartheta_{21} + \beta_{12}\vartheta_{21}\vartheta'_{21} + \beta_{08}\vartheta'_{21}\vartheta_{41}] \\
& + \frac{1}{2} (\beta_{0a} + \beta_{0b})\vartheta_{61} + \frac{1}{2} i (\beta_{23}\vartheta'_{61} + \beta_{0d}\vartheta_{81}). \quad (\text{C9o})
\end{aligned}$$

#### Appendix D: Conserved stress-energy constructed in the FFF

Typically when considering the motion of extended compact bodies, we specify their multipole structure and CM. This specifies the structure of the stress-energy. The equations of motion that determine the worldline follow from the conservation of stress-energy — which we then solve. This is the approach of the Mathisson-Papapetrou-Dixon equations. In this work, we reverse the logic. We construct worldlines resembling two point particles of equal mass in a circular Newtonian orbit whose CM is in free fall. We ask that the stress-energy resembles that of two free point particles up to an interaction term. We then write down the interaction term that conserves the stress-energy to the order that we require.

We can take the metric to be the Minkowski metric  $(\eta_{\alpha\beta})$  in the FFF coordinates  $\tilde{x}^\alpha = (\tilde{t}, \tilde{x}, \tilde{y}, \tilde{z})$  to  $\mathcal{O}(\tilde{x}^\alpha \tilde{x}^\beta)$  [115];

$$ds^2 = (\eta_{\alpha\beta} + h_{\alpha\beta}) d\tilde{x}^\alpha d\tilde{x}^\beta. \quad (\text{D1})$$

The worldline of each body in the IB is

$$z_i^\mu = \left( \tau, (-1)^i \frac{d}{2} \cos \omega_{IB} \tau, 0, (-1)^i \frac{d}{2} \sin \omega_{IB} \tau \right). \quad (\text{D2})$$

We define  $\dot{z}_i^\mu = \frac{dz_i^\mu}{d\tau}$  while  $\frac{dz_i^\mu}{d\tau_i} = \dot{z}_i^\mu \frac{d\tau}{d\tau_i}$ . We impose the timelike normalisation of the tangent vector of each worldline, which implies

$$\frac{d\tau}{d\tau_i} = \left( 1 - h_{\tilde{t}\tilde{t}}|_{z_i} - \left( \frac{d\omega_{IB}}{2} \right)^2 \right)^{-2} + \mathcal{O}(d^3), \quad (\text{D3})$$

having partially expanded in  $d$  at fixed  $\omega_{IB}$ . Now consider the monopole stress-energy term

$$T_i^{\mu\nu} = m_i \int \left( \frac{d\tau}{d\tau_i} \right)^2 \dot{z}_i^\mu \dot{z}_i^\nu \frac{\delta^4(\tilde{x}^\alpha - z_i^\alpha)}{\sqrt{-g}} d\tau_i. \quad (\text{D4})$$

By itself, it is not conserved given our constructed worldline:

$$\nabla_\nu T_i^{\mu\nu} \doteq m_i \int \left( \frac{d\tau}{d\tau_i} \right) \dot{z}_i^\mu \dot{z}_i^\nu \partial_\nu \frac{\delta^4(\tilde{x}^\alpha - z_i^\alpha)}{\sqrt{-g}} d\tau + \mathcal{O}(m_i d^3), \quad (\text{D5})$$

where the dot on the equals sign is to signal that this statement is specialised to the FFF since we have used the fact that the Christoffel connection is  $\mathcal{O}(\tilde{x}^\alpha)$ . By the chain rule

$$\frac{d}{d\tau_i} \delta^4(x^\alpha - z_i^\alpha(\tau_i)) = -\frac{d\tau}{d\tau_i} \dot{z}_i^\nu \partial_\nu \delta^4(x^\alpha - z_i^\alpha(\tau_i)), \quad (\text{D6})$$

thus

$$\nabla_\nu T_i^{\mu\nu} \doteq -m_i \int \dot{z}_i^\mu \frac{d}{d\tau} \frac{\delta^4(\tilde{x}^\alpha - z_i^\alpha)}{\sqrt{-g}} d\tau + \mathcal{O}(m_i d^3). \quad (\text{D7})$$

Integrating by parts and discarding the (vanishing) boundary term, we have

$$\begin{aligned}
\nabla_\nu T_i^{\mu\nu} & \doteq m_i \int \dot{z}_i^\mu \frac{\delta^4(\tilde{x}^\alpha - z_i^\alpha)}{\sqrt{-g}} d\tau + \mathcal{O}(d^3), \\
& \doteq m_i \int \dot{z}_i^\mu \frac{\delta^3(\tilde{x}^\alpha - z_i^\alpha) \delta(\tilde{t} - \tau)}{\sqrt{-g}} d\tau + \mathcal{O}(m_i d^3), \quad (\text{D8})
\end{aligned}$$

for  $\tilde{x}^a = (\tilde{x}, \tilde{y}, \tilde{z})$ . Clearly this equation becomes trivially satisfied if the trajectories are instead geodesics of the Minkowski metric. We now expand the delta function in small  $d$  at fixed  $\omega_{IB}$ ;

$$\nabla_\nu T_i^{\mu\nu} \doteq m_i \int \dot{z}_i^\mu (\delta^3(\tilde{x}^a) - z_i^a \partial_a \delta^3(\tilde{x}^a)) \frac{\delta(\tilde{t} - \tau)}{\sqrt{-g}} d\tau + \mathcal{O}(m_i d^3). \quad (\text{D9})$$

In the sum of two monopole particles with equal masses  $m_i = \mu/2$ ;

$$\sum_i \nabla_\nu T_i^{\mu\nu} \doteq -\mu \int \dot{z}_i^\mu z_i^a \partial_a \delta^3(\tilde{x}^a) \frac{\delta(\tilde{t} - \tau)}{\sqrt{-g}} d\tau + \mathcal{O}(\mu d^3), \quad (\text{D10})$$

since our constructed trajectories satisfy  $\dot{z}_i^{\tilde{t}} \doteq 0$ ,  $\dot{z}_1^a \doteq -\dot{z}_2^a$  and  $z_1^a \doteq -z_2^a$ . We now look for a correction to the stress-energy tensor so that it is conserved to  $\mathcal{O}(\mu d^3)$ . We use the relation

$$P^\mu{}_\nu \dot{z}_i^\nu \doteq -\omega_{IB}^2 P^\mu{}_\nu z_i^\nu, \quad (\text{D11})$$

that follows from Eq. (D2), having defined the projection operator

$$P^\mu{}_\nu \equiv \delta^\mu{}_\nu - \tilde{t}^\mu \tilde{t}_\nu, \quad (\text{D12})$$

and the vector  $\tilde{t}^\nu \doteq (1, 0, 0, 0)$ . Then

$$T_{\text{Int}}^{\mu\nu} \doteq -\mu\omega_{IB}^2 \int P^\mu{}_\alpha z_i^\alpha P^\nu{}_\beta z_i^\beta \frac{\delta^4(\tilde{x}^\alpha - z_c^\alpha)}{\sqrt{-g}} d\tau + \mathcal{O}(\mu d^3),$$

is the required interaction term in the stress-energy to ensure its conservation though  $\mathcal{O}(\mu d^3)$  at fixed  $\omega_{IB}$  having also introduced  $z_c^\alpha \doteq \tau \tilde{t}^\alpha$  as the centre-of-mass worldline. Instead of using the projections, we could also write

$$T_{\text{Int}}^{\mu\nu} \doteq -\mu\omega_{IB}^2 \int (z_i^\mu - z_c^\mu)(z_i^\nu - z_c^\nu) \frac{\delta^4(\tilde{x}^\alpha - z_c^\alpha)}{\sqrt{-g}} d\tau + \mathcal{O}(\mu d^3), \quad (\text{D13})$$

and we notice the trace of this term could be neatly expressed in terms of Synge's world function at this order.

The approximated total stress-energy including the interaction term is

$$T^{\mu\nu} = \mu \int \dot{z}_i^\mu \dot{z}_i^\nu \frac{\delta^4(\tilde{x}^\alpha - z_c^\alpha)}{\sqrt{-g}} d\tau + T_{\text{Int}}^{\mu\nu} + \mathcal{O}(\mu d^3). \quad (\text{D14})$$

We can now compute the stress-energy of the IB in an arbitrary coordinate system. In hindsight, the form of the interaction term is not so mysterious — it is reminiscent of the Newtonian point particle rotational energy,  $\mu\omega_{IB}^2 r^2$ , in which  $r$  is the distance to the axis of rotation. As  $d \rightarrow 0$ , we recover the stress-energy of a free monopole particle of mass  $\mu$ . As a final remark, constructing such a conserved stress-energy tensor may seem arduous in the general case (un-equal mass eccentric IBs). However the relevant stress-energy tensor can also be constructed from the variation of the Lagrangian defined in Ref. [77, 78] (see e.g Chapter 4 of Ref. [115]).

- 
- [1] P. Amaro-Seoane, Relativistic dynamics and extreme mass ratio inspirals, *Living Reviews in Relativity* **21**, 4 (2018), arXiv:1205.5240 [astro-ph.CO].
  - [2] M. Colpi *et al.*, LISA Definition Study Report (2024), arXiv:2402.07571 [astro-ph.CO].
  - [3] W.-R. Hu and Y.-L. Wu, The Taiji Program in Space for gravitational wave physics and the nature of gravity, *National Science Review* **4**, 685 (2017), <https://academic.oup.com/nsr/article-pdf/4/5/685/31566708/nwx116.pdf>.
  - [4] J. Luo *et al.*, TianQin: a space-borne gravitational wave detector, *Classical and Quantum Gravity* **33**, 035010 (2016), arXiv:1512.02076 [astro-ph.IM].
  - [5] E.-K. Li *et al.*, Gravitational Wave Astronomy With TianQin (2024), arXiv:2409.19665 [astro-ph.GA].
  - [6] T. Hinderer and E. E. Flanagan, Two-timescale analysis of extreme mass ratio inspirals in Kerr spacetime: Orbital motion, *Phys. Rev. D* **78**, 064028 (2008).
  - [7] N. A. Collins and S. A. Hughes, Towards a formalism for mapping the spacetimes of massive compact objects: Bumpy black holes and their orbits, *Phys. Rev. D* **69**, 124022 (2004).
  - [8] S. J. Vigeland and S. A. Hughes, Spacetime and orbits of bumpy black holes, *Phys. Rev. D* **81**, 024030 (2010).
  - [9] C. Berry *et al.*, The unique potential of extreme mass-ratio inspirals for gravitational-wave astronomy, *Bulletin of the American Astronomical Society* **51**, 42 (2019), arXiv:1903.03686 [astro-ph.HE].
  - [10] T.-G. Zi, J.-D. Zhang, H.-M. Fan, X.-T. Zhang, Y.-M. Hu, C. Shi, and J. Mei, Science with the TianQin Observatory: Preliminary results on testing the no-hair theorem with extreme mass ratio inspirals, *Phys. Rev. D* **104**, 064008 (2021), arXiv:2104.06047 [gr-qc].
  - [11] S. Babak, J. Gair, A. Sesana, E. Barausse, C. F. Sopuerta, C. P. L. Berry, E. Berti, P. Amaro-Seoane, A. Petiteau, and A. Klein, Science with the space-based interferometer LISA. V: Extreme mass-ratio inspirals, *Phys. Rev. D* **95**, 103012 (2017), arXiv:1703.09722 [gr-qc].
  - [12] L. Barack and C. Cutler, LISA capture sources: Approximate waveforms, signal-to-noise ratios, and parameter estimation accuracy, *Phys. Rev. D* **69**, 082005 (2004), arXiv:gr-qc/0310125.
  - [13] A. J. K. Chua and J. R. Gair, Improved analytic extreme-mass-ratio inspiral model for scoping out eLISA data analysis, *Classical and Quantum Gravity* **32**, 232002 (2015), arXiv:1510.06245 [gr-qc].
  - [14] R. Fujita and M. Shibata, Extreme mass ratio inspirals on the equatorial plane in the adiabatic order, *Phys. Rev. D* **102**, 064005 (2020), arXiv:2008.13554 [gr-qc].
  - [15] A. J. K. Chua *et al.*, Rapid Generation of Fully Relativistic Extreme-Mass-Ratio-Inspiral Waveform Templates for LISA Data Analysis, *Phys. Rev. Lett.* **126**, 051102 (2021), arXiv:2008.06071 [gr-qc].
  - [16] M. L. Katz, A. J. K. Chua, L. Speri, N. Warburton, and S. A. Hughes, Fast extreme-mass-ratio-inspiral waveforms: New tools for millihertz gravitational-wave data analysis, *Phys. Rev. D* **104**, 064047 (2021), arXiv:2104.04582 [gr-qc].
  - [17] S. A. Hughes, N. Warburton, G. Khanna, A. J. K. Chua, and M. L. Katz, Adiabatic waveforms for extreme mass-ratio inspirals via multivoice decomposition in time and frequency, *Phys. Rev. D* **103**, 104014 (2021), arXiv:2102.02713 [gr-qc].
  - [18] S. Isoyama *et al.*, Adiabatic Waveforms from Extreme-Mass-Ratio Inspirals: An Analytical Approach, *Phys. Rev. Lett.* **128**, 231101 (2022), arXiv:2111.05288 [gr-qc].
  - [19] B. Wardell, A. Pound, N. Warburton, J. Miller, L. Durkan, and A. Le Tiec, Gravitational Waveforms for Compact Binaries from Second-Order Self-Force Theory, *Phys. Rev. Lett.* **130**, 241402 (2023), arXiv:2112.12265 [gr-qc].
  - [20] L. Speri, M. L. Katz, A. J. K. Chua, S. A. Hughes, N. Warburton, J. E. Thompson, C. E. A. Chapman-Bird, and J. R. Gair, Fast and Fourier: Extreme Mass Ratio Inspiral Waveforms in the Frequency Do-



- main, *Front. Appl. Math. Stat.* **9**, 1266739 (2023), [arXiv:2307.12585 \[gr-qc\]](#).
- [21] S. Babak, H. Fang, J. R. Gair, K. Glampedakis, and S. A. Hughes, 'Kludge' gravitational waveforms for a test-body orbiting a Kerr black hole, *Phys. Rev. D* **75**, 024005 (2007), [Erratum: *Phys.Rev.D* 77, 04990 (2008)], [arXiv:gr-qc/0607007](#).
- [22] Z. Nasipak, Adiabatic gravitational waveform model for compact objects undergoing quasicircular inspirals into rotating massive black holes, *Phys. Rev. D* **109**, 044020 (2024), [arXiv:2310.19706 \[gr-qc\]](#).
- [23] A. Albertini, R. Gamba, A. Nagar, and S. Bernuzzi, Effective-one-body waveforms for extreme-mass-ratio binaries: Consistency with second-order gravitational self-force quasicircular results and extension to non-precessing spins and eccentricity, *Phys. Rev. D* **109**, 044022 (2024), [arXiv:2310.13578 \[gr-qc\]](#).
- [24] W.-B. Han, Gravitational radiation from a spinning compact object around a supermassive Kerr black hole in circular orbit, *Phys. Rev. D* **82**, 084013 (2010), [arXiv:1008.3324 \[gr-qc\]](#).
- [25] G. A. Piovano, A. Maselli, and P. Pani, Extreme mass ratio inspirals with spinning secondary: A detailed study of equatorial circular motion, *Phys. Rev. D* **102**, 024041 (2020), [arXiv:2004.02654 \[gr-qc\]](#).
- [26] L. V. Drummond and S. A. Hughes, Precisely computing bound orbits of spinning bodies around black holes. I. General framework and results for nearly equatorial orbits, *Phys. Rev. D* **105**, 124040 (2022), [arXiv:2201.13334 \[gr-qc\]](#).
- [27] L. V. Drummond and S. A. Hughes, Precisely computing bound orbits of spinning bodies around black holes. II. Generic orbits, *Phys. Rev. D* **105**, 124041 (2022), [arXiv:2201.13335 \[gr-qc\]](#).
- [28] G. A. Piovano, R. Brito, A. Maselli, and P. Pani, Assessing the detectability of the secondary spin in extreme mass-ratio inspirals with fully relativistic numerical waveforms, *Phys. Rev. D* **104**, 124019 (2021), [arXiv:2105.07083 \[gr-qc\]](#).
- [29] V. Skoupý and G. Lukes-Gerakopoulos, Spinning test body orbiting around a Kerr black hole: Eccentric equatorial orbits and their asymptotic gravitational-wave fluxes, *Phys. Rev. D* **103**, 104045 (2021), [arXiv:2102.04819 \[gr-qc\]](#).
- [30] M. Rahman and A. Bhattacharyya, Prospects for determining the nature of the secondaries of extreme mass-ratio inspirals using the spin-induced quadrupole deformation, *Phys. Rev. D* **107**, 024006 (2023), [arXiv:2112.13869 \[gr-qc\]](#).
- [31] J. Mathews, A. Pound, and B. Wardell, Self-force calculations with a spinning secondary, *Phys. Rev. D* **105**, 084031 (2022), [arXiv:2112.13069 \[gr-qc\]](#).
- [32] V. Skoupý and G. Lukes-Gerakopoulos, Adiabatic equatorial inspirals of a spinning body into a Kerr black hole, *Phys. Rev. D* **105**, 084033 (2022), [arXiv:2201.07044 \[gr-qc\]](#).
- [33] L. V. Drummond, P. Lynch, A. G. Hanselman, D. R. Becker, and S. A. Hughes, Extreme mass-ratio inspiral and waveforms for a spinning body into a Kerr black hole via osculating geodesics and near-identity transformations, *Phys. Rev. D* **109**, 064030 (2024), [arXiv:2310.08438 \[gr-qc\]](#).
- [34] V. Skoupy, G. Lukes-Gerakopoulos, L. V. Drummond, and S. A. Hughes, Asymptotic gravitational-wave fluxes from a spinning test body on generic orbits around a Kerr black hole, *Phys. Rev. D* **108**, 044041 (2023), [arXiv:2303.16798 \[gr-qc\]](#).
- [35] O. Burke, G. A. Piovano, N. Warburton, P. Lynch, L. Speri, C. Kavanagh, B. Wardell, A. Pound, L. Durkan, and J. Miller, Assessing the importance of first postadiabatic terms for small-mass-ratio binaries, *Phys. Rev. D* **109**, 124048 (2024), [arXiv:2310.08927 \[gr-qc\]](#).
- [36] V. Skoupý and V. Witzany, Post-Newtonian expansions of extreme mass ratio inspirals of spinning bodies into Schwarzschild black holes (2024), [arXiv:2406.14291 \[gr-qc\]](#).
- [37] A. Albertini, A. Nagar, J. Mathews, and G. Lukes-Gerakopoulos, Comparing second-order gravitational self-force and effective-one-body waveforms from inspiralling, quasicircular black hole binaries with a nonspinning primary and a spinning secondary, *Phys. Rev. D* **110**, 044034 (2024), [arXiv:2406.04108 \[gr-qc\]](#).
- [38] G. A. Piovano, C. Pantelidou, J. Mac Uilliam, and V. Witzany, Spinning particles near Kerr black holes: Orbits and gravitational-wave fluxes through the Hamilton-Jacobi formalism (2024), [arXiv:2410.05769 \[gr-qc\]](#).
- [39] E. Addison, P. Laguna, and S. Larson, Busting Up Binaries: Encounters Between Compact Binaries and a Supermassive Black Hole (2015), [arXiv:1501.07856 \[astro-ph.HE\]](#).
- [40] X. Chen and W.-B. Han, Extreme-mass-ratio inspirals produced by tidal capture of binary black holes, *Communications Physics* **1**, 53 (2018), [arXiv:1801.05780 \[astro-ph.HE\]](#).
- [41] J. M. Bellovary *et al.*, Migration Traps in Disks around Supermassive Black Holes, *APJL* **819**, L17 (2016), [arXiv:1511.00005 \[astro-ph.GA\]](#).
- [42] P. Peng and X. Chen, The last migration trap of compact objects in AGN accretion disc, *MNRAS* **505**, 1324 (2021), [arXiv:2104.07685 \[astro-ph.HE\]](#).
- [43] H. Tagawa, Z. Haiman, and B. Kocsis, Formation and Evolution of Compact-object Binaries in AGN Disks, *Astrophys. J.* **898**, 25 (2020), [arXiv:1912.08218 \[astro-ph.GA\]](#).
- [44] Z. Pan and H. Yang, Formation Rate of Extreme Mass Ratio Inspirals in Active Galactic Nuclei, *Phys. Rev. D* **103**, 103018 (2021), [arXiv:2101.09146 \[astro-ph.HE\]](#).
- [45] P. Amaro-Seoane *et al.*, Astrophysics with the Laser Interferometer Space Antenna, *Living Reviews in Relativity* **26**, 2 (2023), [arXiv:2203.06016 \[gr-qc\]](#).
- [46] R. Abbott *et al.* (LIGO Scientific, Virgo), Gw190521: A binary black hole merger with a total mass of  $150 M_{\odot}$ , *Phys. Rev. Lett.* **125**, 101102 (2020).
- [47] R. Abbott *et al.* (LIGO Scientific, Virgo), GWTC-2: Compact Binary Coalescences Observed by LIGO and Virgo during the First Half of the Third Observing Run, *Physical Review X* **11**, 021053 (2021), [arXiv:2010.14527 \[gr-qc\]](#).
- [48] C. D. Bailyn *et al.*, The Mass Distribution of Stellar Black Holes, *Astrophys. J.* **499**, 367 (1998), [arXiv:astro-ph/9708032 \[astro-ph\]](#).
- [49] C. L. Fryer and V. Kalogera, Theoretical Black Hole Mass Distributions, *Astrophys. J.* **554**, 548 (2001), [arXiv:astro-ph/9911312 \[astro-ph\]](#).
- [50] X. Chen, S. Li, and Z. Cao, Mass-redshift degeneracy for the gravitational-wave sources in the vicinity

- of supermassive black holes, *MNRAS* **485**, L141 (2019), arXiv:1703.10543 [astro-ph.HE].
- [51] M. J. Graham *et al.*, Candidate electromagnetic counterpart to the binary black hole merger gravitational-wave event s190521g, *Phys. Rev. Lett.* **124**, 251102 (2020).
- [52] R. Abbott *et al.* (LIGO Scientific, Virgo), Properties and Astrophysical Implications of the 150  $M_{\odot}$  Binary Black Hole Merger GW190521, *APJL* **900**, L13 (2020), arXiv:2009.01190 [astro-ph.HE].
- [53] M. Silva and C. Hirata, Dynamical perturbations around an extreme mass ratio inspiral near resonance, *Phys. Rev. D* **106**, 084058 (2022), arXiv:2207.07733 [gr-qc].
- [54] Y. Meiron, B. Kocsis, and A. Loeb, Detecting Triple Systems with Gravitational Wave Observations, *APJ* **834**, 200 (2017), arXiv:1604.02148 [astro-ph.HE].
- [55] W.-B. Han and X. Chen, Testing general relativity using binary extreme-mass-ratio inspirals, *MNRAS* **485**, L29 (2019), arXiv:1801.07060 [gr-qc].
- [56] L. Randall and Z.-Z. Xianyu, A Direct Probe of Mass Density near Inspiring Binary Black Holes, *APJ* **878**, 75 (2019), arXiv:1805.05335 [gr-qc].
- [57] K. W. K. Wong, V. Baibhav, and E. Berti, Binary radial velocity measurements with space-based gravitational-wave detectors, *MNRAS* **488**, 5665 (2019), arXiv:1902.01402 [astro-ph.HE].
- [58] X. Zhang and X. Chen, The appearance of a merging binary black hole very close to a spinning supermassive black hole, *MNRAS* **521**, 2919 (2023), arXiv:2302.04015 [astro-ph.HE].
- [59] A. Torres-Orjuela *et al.*, Detecting the beaming effect of gravitational waves, *Phys. Rev. D* **100**, 063012 (2019), arXiv:1806.09857 [astro-ph.HE].
- [60] H. Yan, X. Chen, and A. Torres-Orjuela, Calculating the gravitational waves emitted from high-speed sources, *Phys. Rev. D* **107**, 103044 (2023), arXiv:2305.04969 [gr-qc].
- [61] J. M. Ezquiaga *et al.*, Phase effects from strong gravitational lensing of gravitational waves, *Phys. Rev. D* **103**, 064047 (2021), arXiv:2008.12814 [gr-qc].
- [62] M. Pijenburg, G. Cusin, C. Pitrou, and J.-P. Uzan, Wave optics lensing of gravitational waves: Theory and phenomenology of triple systems in the lisa band, *Phys. Rev. D* **110**, 044054 (2024).
- [63] V. Cardoso, F. Duque, and G. Khanna, Gravitational tuning forks and hierarchical triple systems, *Phys. Rev. D* **103**, L081501 (2021).
- [64] Y. Fang, R.-Z. Guo, and Q.-G. Huang, Tests for the existence of horizon through gravitational waves from a small binary in the vicinity of a massive object, *Physics Letters B* **822**, 136654 (2021), arXiv:2108.04511 [astro-ph.CO].
- [65] Y. Jiang *et al.*, Distinguishability of binary extreme-mass-ratio inspirals in low frequency band, *European Physical Journal C* **84**, 478 (2024).
- [66] M. Mathisson, Neue mechanik materieller systemes, *Acta Phys. Polon.* **6**, 163 (1937).
- [67] M. Mathisson, Republication of: New mechanics of material systems, *Gen. Rel. Grav.* **42**, 1011 (2010).
- [68] A. Papapetrou, Spinning test particles in general relativity. I., *Proc. Roy. Soc. Lond. A* **209**, 248 (1951).
- [69] W. G. Dixon, Dynamics of extended bodies in general relativity. II. Moments of the charge-current vector, *Proc. Roy. Soc. Lond. A* **319**, 509 (1970).
- [70] W. G. Dixon, Dynamics of extended bodies in general relativity III. Equations of motion, *Phil. Trans. Roy. Soc. Lond. A* **277**, 59 (1974).
- [71] A. I. Harte, Mechanics of extended masses in general relativity, *Class. Quant. Grav.* **29**, 055012 (2012), arXiv:1103.0543 [gr-qc].
- [72] Y. Jiang and W.-B. Han, General formalism for dirty extreme-mass-ratio inspirals, *Sci. China Phys. Mech. Astron.* **67**, 270411 (2024).
- [73] K. Meng, H. Zhang, X.-L. Fan, and Y. Yong, Distinguish the EMRI and B-EMRI system by gravitational waves (2024), arXiv:2405.07113 [gr-qc].
- [74] E. Berti, V. Cardoso, and A. O. Starinets, TOPICAL REVIEW: Quasinormal modes of black holes and black branes, *Classical and Quantum Gravity* **26**, 163001 (2009), arXiv:0905.2975 [gr-qc].
- [75] X. Chen and Z. Zhang, Binaries wandering around supermassive black holes due to gravitoelectromagnetism, *Phys. Rev. D* **106**, 103040 (2022), arXiv:2206.08104 [astro-ph.HE].
- [76] F. Camilloni, G. Grignani, T. Harmark, R. Oliveri, M. Orselli, and D. Pica, Tidal deformations of a binary system induced by an external kerr black hole, *Phys. Rev. D* **107**, 084011 (2023).
- [77] K.-i. Maeda, P. Gupta, and H. Okawa, Chaotic von zeipel-lidov-kozai oscillations of a binary system around a rotating supermassive black hole, *Phys. Rev. D* **108**, 123041 (2023).
- [78] A. Gorbatsievich and A. Bobrik, The Equations of Motion of Compact Binaries in the Neighborhood of Supermassive Black Hole, *AIP Conference Proceedings* **1205**, 87 (2010).
- [79] R. H. Boyer and R. W. Lindquist, Maximal Analytic Extension of the Kerr Metric, *Journal of Mathematical Physics* **8**, 265 (1967).
- [80] D. Bini, A. Geralico, and R. T. Jantzen, Kerr metric, static observers and Fermi coordinates, *Classical and Quantum Gravity* **22**, 4729 (2005), arXiv:gr-qc/0510023 [gr-qc].
- [81] D. Klein and P. Collas, General transformation formulas for Fermi Walker coordinates, *Classical and Quantum Gravity* **25**, 145019 (2008), arXiv:0712.3838 [gr-qc].
- [82] A. Pound and B. Wardell, Black hole perturbation theory and gravitational self-force (2021), arXiv:2101.04592 [gr-qc].
- [83] N. Afshordi *et al.* (LISA Consortium Waveform Working Group), Waveform Modelling for the Laser Interferometer Space Antenna (2023), arXiv:2311.01300 [gr-qc].
- [84] C. W. Misner, K. S. Thorne, and J. A. Wheeler, *Gravitation* (1973).
- [85] B. Carter, Global structure of the kerr family of gravitational fields, *Phys. Rev.* **174**, 1559 (1968).
- [86] R. Fujita and W. Hikida, Analytical solutions of bound timelike geodesic orbits in kerr spacetime, *Classical and Quantum Gravity* **26**, 135002 (2009).
- [87] W. Rindler and V. Perlick, Rotating coordinates as tools for calculating circular geodesics and gyroscopic precession, *General Relativity and Gravitation* **22**, 1067 (1990).
- [88] M. Sasaki and H. Tagoshi, Analytic Black Hole Perturbation Approach to Gravitational Radiation, *Living Reviews in Relativity* **6**, 6 (2003), arXiv:gr-qc/0306120 [gr-qc].

- [89] R. Fujita and W. Hikida, Analytical solutions of bound timelike geodesic orbits in Kerr spacetime, *Classical and Quantum Gravity* **26**, 135002 (2009), arXiv:0906.1420 [gr-qc].
- [90] S. Drasco and S. A. Hughes, Gravitational wave snapshots of generic extreme mass ratio inspirals, *Phys. Rev. D* **73**, 024027 (2006), arXiv:gr-qc/0509101 [gr-qc].
- [91] R. Fujita, W. Hikida, and H. Tagoshi, An Efficient Numerical Method for Computing Gravitational Waves Induced by a Particle Moving on Eccentric Inclined Orbits around a Kerr Black Hole, *Prog. Theor. Phys.* **121**, 843 (2009), arXiv:0904.3810 [gr-qc].
- [92] S. A. Teukolsky, Rotating black holes - separable wave equations for gravitational and electromagnetic perturbations, *Phys. Rev. Lett.* **29**, 1114 (1972).
- [93] S. A. Teukolsky, Perturbations of a Rotating Black Hole. I. Fundamental Equations for Gravitational, Electromagnetic, and Neutrino-Field Perturbations, *Astrophys. J.* **185**, 635 (1973).
- [94] E. Newman and R. Penrose, An Approach to Gravitational Radiation by a Method of Spin Coefficients, *Journal of Mathematical Physics* **3**, 566 (1962).
- [95] S. O'Sullivan and S. A. Hughes, Strong-field tidal distortions of rotating black holes: Formalism and results for circular, equatorial orbits, *Phys. Rev. D* **90**, 124039 (2014), arXiv:1407.6983 [gr-qc].
- [96] T. Apostolatos, D. Kennefick, A. Ori, and E. Poisson, Gravitational radiation from a particle in circular orbit around a black hole. iii. stability of circular orbits under radiation reaction, *Phys. Rev. D* **47**, 5376 (1993).
- [97] D. Kennefick and A. Ori, Radiation reaction induced evolution of circular orbits of particles around Kerr black holes, *Phys. Rev. D* **53**, 4319 (1996), arXiv:gr-qc/9512018.
- [98] Y. Mino, M. Sasaki, M. Shibata, H. Tagoshi, and T. Tanaka, Black hole perturbation: Chapter 1, *Prog. Theor. Phys. Suppl.* **128**, 1 (1997), arXiv:gr-qc/9712057.
- [99] F. D. Ryan, Effect of gravitational radiation reaction on circular orbits around a spinning black hole, *Phys. Rev. D* **52**, R3159 (1995), arXiv:gr-qc/9506023.
- [100] S. Mano, H. Suzuki, and E. Takasugi, Analytic Solutions of the Teukolsky Equation and Their Low Frequency Expansions, *Progress of Theoretical Physics* **95**, 1079 (1996), <https://academic.oup.com/ptp/article-pdf/95/6/1079/5282662/95-6-1079.pdf>.
- [101] R. Fujita and H. Tagoshi, New Numerical Methods to Evaluate Homogeneous Solutions of the Teukolsky Equation, *Progress of Theoretical Physics* **112**, 415 (2004), <https://academic.oup.com/ptp/article-pdf/112/3/415/5382220/112-3-415.pdf>.
- [102] R. Fujita and H. Tagoshi, New Numerical Methods to Evaluate Homogeneous Solutions of the Teukolsky Equation. II: — Solutions of the Continued Fraction Equation —, *Progress of Theoretical Physics* **113**, 1165 (2005), <https://academic.oup.com/ptp/article-pdf/113/6/1165/5285582/113-6-1165.pdf>.
- [103] M. Sasaki and T. Nakamura, Gravitational Radiation from a Kerr Black Hole. I. Formulation and a Method for Numerical Analysis, *Progress of Theoretical Physics* **67**, 1788 (1982), <https://academic.oup.com/ptp/article-pdf/67/6/1788/5332324/67-6-1788.pdf>.
- [104] R. K. L. Lo, Recipes for computing radiation from a Kerr black hole using Generalized Sasaki-Nakamura formalism: I. Homogeneous solutions (2023), arXiv:2306.16469 [gr-qc].
- [105] J. M. Bardeen, W. H. Press, and S. A. Teukolsky, Rotating Black Holes: Locally Nonrotating Frames, Energy Extraction, and Scalar Synchrotron Radiation, *Astrophys. J.* **178**, 347 (1972).
- [106] W. H. Press, B. P. Flannery, and S. A. Teukolsky, *Numerical recipes. The art of scientific computing* (1986).
- [107] U. Ruangsri and S. A. Hughes, Census of transient orbital resonances encountered during binary inspiral, *Phys. Rev. D* **89**, 084036 (2014), arXiv:1307.6483 [gr-qc].
- [108] P. Lynch *et al.*, Fast inspirals and the treatment of orbital resonances, arXiv e-prints, arXiv:2405.21072 (2024), arXiv:2405.21072 [gr-qc].
- [109] L. Stein, qnm: A Python package for calculating Kerr quasinormal modes, separation constants, and spherical-spheroidal mixing coefficients, *The Journal of Open Source Software* **4**, 1683 (2019), arXiv:1908.10377 [gr-qc].
- [110] J. G. Hills, Hyper-velocity and tidal stars from binaries disrupted by a massive Galactic black hole, *Nature (London)* **331**, 687 (1988).
- [111] Y. Kozai, Secular perturbations of asteroids with high inclination and eccentricity, *AJ* **67**, 591 (1962).
- [112] M. L. Lidov, The evolution of orbits of artificial satellites of planets under the action of gravitational perturbations of external bodies, *PLANSS* **9**, 719 (1962).
- [113] B. Katz, S. Dong, and R. Malhotra, Long-term cycling of kozai-lidov cycles: Extreme eccentricities and inclinations excited by a distant eccentric perturber, *Phys. Rev. Lett.* **107**, 181101 (2011).
- [114] J. M. O. Antognini, Timescales of Kozai-Lidov oscillations at quadrupole and octupole order in the test particle limit, *MNRAS* **452**, 3610 (2015), arXiv:1504.05957 [astro-ph.EP].
- [115] E. Poisson, *A Relativist's Toolkit: The Mathematics of Black-Hole Mechanics* (Cambridge University Press, 2009).